

PMA-Diffusion: A Physics-guided Mask-Aware Diffusion Framework for Traffic State Estimation from Sparse Observations

Lindong Liu^a, Zhixiong Jin^b and Seongjin Choi^{a,*}

^aDepartment of Civil, Environmental, and Geo- Engineering, University of Minnesota, 500 Pillsbury Dr. SE, Minneapolis, MN 55455, USA

^bUniv. Gustave Eiffel, ENTPe, EMob-Lab, Lyon, F-69675, France

ARTICLE INFO

Keywords:

Traffic state estimation
Intelligent Transportation Systems
Diffusion models
Physics-Informed Machine Learning
Sparse sensing
Inverse problem

Abstract

High-resolution highway traffic state information is essential for Intelligent Transportation Systems, but typical traffic data acquired from loop detectors and probe vehicles are often too sparse and noisy to capture the detailed dynamics of traffic flow. We propose PMA-Diffusion, a physics-guided mask-aware diffusion framework that reconstructs unobserved highway speed fields from sparse, incomplete observations. Our approach trains a diffusion prior directly on sparsely observed speed fields using two mask-aware training strategies: Single-Mask and Double-Mask. At the inference phase, the physics-guided posterior sampler alternates reverse-diffusion updates, observation projection, and physics-guided projection based on adaptive anisotropic smoothing to reconstruct the missing speed fields. The proposed framework is tested on the I-24 MOTION dataset with varying visibility ratios. Even under severe sparsity, with only 5% visibility, PMA-Diffusion outperforms other baselines across three reconstruction error metrics. Furthermore, PMA-diffusion trained with sparse observation nearly matches the performance of the baseline model trained on fully observed speed fields. The results indicate that combining mask-aware diffusion priors with a physics-guided posterior sampler provides a reliable and flexible solution for traffic state estimation under realistic sensing sparsity.

1. Introduction

High-resolution traffic state information is essential for both transportation operations and research. It supports Advanced Transportation Management Systems (e.g., ramp metering (Belletti et al., 2017), variable speed limits (Zhang et al., 2025b), coordinated traffic signal control (Ahmed et al., 2019), and incident detection (Coursey et al., 2025)) and Advanced Traveler Information Systems (e.g., travel time reliability measures (Liu et al., 2004), dynamic route planning (Ahmed et al., 2016), and traveler advisories (Liebig et al., 2017; Mori et al., 2015)). It also provides transportation researchers with detailed insights into various traffic phenomena, such as congestion dynamics, bottleneck formation, and the propagation of traffic waves (Ji et al., 2026). However, obtaining such high-resolution observations at scale remains challenging. In practice, most highway monitoring systems highly rely on sparse loop detectors (installed approximately half-mile intervals (Liu et al., 2006; Minnesota Department of Transportation, 2019)), which provide consistent but location-limited measurements, or probe vehicles that provide broader spatial coverage but suffer from low and uneven penetration rates (typically 2-5% penetration rate (Seo et al., 2017; Herrera et al., 2010)). Emerging sensing platforms, such as Unmanned Aerial Vehicles (UAV)-based traffic monitoring (e.g., pNEUMA (Barmounakis and Geroliminis, 2020), Songdo traffic data (Fonod et al., 2025)) and large-scale multi-camera systems (I-24 MOTION testbed (Gloudemans et al., 2023)), can provide near-complete and fine-grained observations but are constrained by battery capacity, altitude restrictions, and privacy regulations, and deployment cost (Butilă and Boboc, 2022). As a result, it is difficult to fully observe traffic states at high resolution, making it necessary to develop methods that can reconstruct them from sparse and incomplete measurements.

Traffic State Estimation (TSE) addresses this problem by reconstructing high-resolution traffic data from sparse and heterogeneous measurements (Wang et al., 2023). Existing methods are often grouped into model-driven and data-driven approaches (Seo et al., 2017). Model-driven methods rely on macroscopic traffic-flow theory, such as the Lighthill-Whitham-Richards (LWR) model and its extensions (Lighthill and Whitham, 1955; Coifman, 2002). These models are interpretable and can extrapolate traffic states from relatively few measurements, but their assumptions,

*Corresponding author

✉ liu03035@umn.edu (L. Liu); zhixiong.jin@univ-eiffel.fr (Z. Jin); chois@umn.edu (S. Choi)

ORCID(s): 0009-0001-7071-7002 (L. Liu); 0000-0002-1370-781X (Z. Jin); 0000-0001-7140-537X (S. Choi)

such as homogeneous traffic conditions and stable wave speeds, often do not hold in the real world (Shi et al., 2021). Data-driven methods instead learn traffic states directly from historical data and can flexibly capture nonlinear spatial-temporal relationships without specifying a detailed traffic-flow model. Even though recent deep learning models can capture complex spatial-temporal dependencies, they typically require high-visibility data and corresponding full ground truth. When the available data are sparse, or when the model is conditioned only on limited observations, the reconstructions can violate basic traffic principles (Thodi et al., 2022).

Recent work on Physics-Informed Deep Learning (PIDL) incorporates traffic theory into the learning objective (Shi et al., 2021; Di et al., 2023). Most PIDL methods use the conservation laws or the fundamental diagram relations by penalizing their Partial Differential Equation (PDE) residuals or adding physics-based regularization terms to the loss (Raissi et al., 2019). When traffic states are fully or densely observed, these physics terms help stabilize training and lead to more reliable estimations (Yuan et al., 2021; Wu et al., 2024). However, such full-observation conditions are rare in practice due to sparse and limited sensor coverage. In addition, physics terms are usually encoded directly in the loss under a fixed detector layout and masking pattern. In other words, when the sensor configuration changes at deployment, the training-time masks no longer match the new observation measurement (Xue et al., 2024).

In summary, current TSE methods share three fundamental limitations. First, most learning-based models **require fully observed traffic states** for model training. For example, previous Variational Autoencoder (VAE) and Diffusion-based generative models rely on complete spatiotemporal speed fields for training (Boquet et al., 2020; Lei et al., 2024; Lu et al., 2025; Zhang et al., 2025a), and Generative Adversarial Network (GAN) based models are trained by matching sparse observations to their corresponding full ground-truth speed data (Zhang et al., 2022; Mo et al., 2022b). Gaussian process (GP)-based approaches provide a principled probabilistic alternative (Yuan et al., 2021; Wu et al., 2024; Storm et al., 2022), but they depend on predefined physics-informed kernels or relatively dense observations for calibration. Second, most existing methods **produce only a single point estimate**, instead of modeling the uncertainty and full posterior distribution of the complete speed field. In sparse sensing regimes, multiple traffic states can be consistent with the same observations, so representing the posterior distribution is important for uncertainty quantification and downstream decision making. This limitation appears in classical reconstruction methods (Treiber and Helbing, 2002; Treiber et al., 2011; Tak et al., 2016; Wang et al., 2023), in the majority of deep regression models (Rempe et al., 2022; Liu et al., 2021), and in many PIDL approaches (Shi et al., 2021; Huang and Agarwal, 2022; Zhang et al., 2024; Shi et al., 2023; Abewickrema et al., 2026; Thodi et al., 2022). GP-based methods *do* provide predictive variances, but these variances are induced by the chosen kernel rather than arising from a learned generative model of traffic dynamics. Third, current PIDL frameworks typically encode the detector layout and observation mask directly into the loss function. Since these physics penalties are tied to the specific observation operator used during training (Huang and Agarwal, 2020; Shi et al., 2023), the learned model **becomes sensitive to changes in detector configuration**.

In this paper, we propose **PMA-Diffusion**, a Physics-guided Mask-Aware Diffusion framework for reconstructing high-resolution traffic speed fields from sparse loop detectors and probe vehicle data. **PMA-Diffusion** addresses the aforementioned three key limitations of existing TSE methods by considering TSE as an inverse problem and decoupling generative prior training and posterior sampling. In the inverse problem formulation, the goal is to recover the unobserved traffic state (\mathbf{x}) from sparse and noisy observation ($\mathbf{y} = \mathcal{A}(\mathbf{x}) + \boldsymbol{\eta}$), where \mathcal{A} denotes the measurement operator (e.g., observation mask) and $\boldsymbol{\eta}$ denotes measurement noise. PMA-Diffusion first learns a prior distribution ($p(\mathbf{x})$) of high-resolution traffic state directly from sparse observations (\mathbf{y}) using Single-mask and Double-mask training strategies. The Single-mask strategy follows the actual sensor visibility pattern, whereas the Double-mask strategy adds an auxiliary mask so that even always-visible locations are occasionally treated as unobserved during training. This removes the dependence on full observation for training. Then, to produce the distribution over all plausible high-resolution traffic states given observation, we design a physics-guided posterior sampling process ($p(\mathbf{x} | \mathbf{y}) \propto p(\mathbf{x}) \cdot p(\mathbf{y} | \mathbf{x})$) (Lugmayr et al., 2022; Chung and Ye, 2024). Specifically, during posterior sampling, PMA-Diffusion alternates reverse-diffusion updates with two projection steps: an observation projection that injects the measured values ($p(\mathbf{y} | \mathbf{x})$) back into the trajectory, and a physics-guided projection that enforces basic kinematic-wave structure on the unobserved regions. Since these projections are applied during inference rather than encoded into the loss, the framework can be used with arbitrary observation masks over highway speed fields.

This paper is organized as follows. Section 2 reviews related work on traffic state estimation. Section 3 describes the methodology of this paper. A detailed problem formulation is presented in Section 3.1, the proposed framework of PMA-Diffusion is presented in Section 3.2 and Section 3.3. Section 4 describes the experiments and evaluations. Section 5 provides conclusions.

2. Background

In this section, we review three lines of work related to our proposed framework: (i) Model-Driven and Data-Driven Approaches for TSE, (ii) Physics-Informed Deep Learning (PIDL) for TSE, and (iii) Diffusion-based Approaches for Inverse Problems and TSE.

2.1. Model-Driven and Data-Driven Approaches for TSE

Early work on TSE was based on traffic flow theory and aimed to reconstruct complete traffic states from sparse sensor measurements. The first group of methods directly relies on macroscopic traffic flow equations, most commonly the LWR model (Lighthill and Whitham, 1955; Richards, 1956) and its discretized form, the Cell Transmission Model (CTM) (Daganzo, 1995). These methods solve the traffic flow PDE and use boundary conditions to estimate the traffic states. For example, Coifman (2002) estimated traffic states using data from a single double-loop detector based on the fundamental diagram relationship. Seo and Kusakabe (2015) incorporated probe vehicle spacing data into the LWR conservation law to infer density and flow in Eulerian coordinates, enabling state estimation under low probe penetration rates. In addition to PDE-based formulations, Treiber and Helbing (2003) proposed the Adaptive Smoothing Method (ASM), which reconstructs spatiotemporal speed fields by applying different smoothing strengths along the characteristic directions of free-flow and congested traffic waves (Treiber and Helbing, 2002; Treiber et al., 2011). A second group of methods rewrites the traffic flow PDE as a dynamic model with a corresponding observation model, allowing recursive estimation through filtering techniques. Following this idea, Wang and Papageorgiou (2005) discretized a second-order traffic flow model (Papageorgiou et al., 1990) into a nonlinear state-space form and applied the Extended Kalman Filter (EKF) to integrate loop detector data for traffic state estimation on highway. Subsequent studies improved performance under nonlinearities and high-dimensional state representations by using the Unscented Kalman Filter (UKF) and the Ensemble Kalman Filter (EnKF) (Mihaylova et al., 2006; Work et al., 2008). Despite their data efficiency and physical interpretability, model-driven methods are highly sensitive to model structure and parameter choices. Offline calibration of fundamental-diagram shape and wave speeds requires large volumes of high-quality historical data and is subject to drift as demand patterns, driver behavior, and control strategies evolve (Yuan et al., 2021; Di et al., 2023).

In contrast, data-driven methods infer traffic states directly from historical data (Seo et al., 2017). Early data-driven studies mainly adopted traditional statistical learning techniques to impute missing traffic measurements. For example, Zhong et al. (2004) employed Auto Regressive Integrated Moving Average (ARIMA) to reconstruct missing data. Ni and Leonard (2005) further addressed uncertainty in missing observations by using Bayesian Networks. Researchers then introduced non-parametric methods that avoid strong functional assumptions. Kernel regression smooths inconsistent measurements using locally weighted averages (Yin et al., 2012), and k-nearest neighbors reconstruct speed or flow by identifying similar historical patterns (Tak et al., 2016). Another line of work uses the low-rank structure of traffic states in space and time: Coric et al. (2012) reconstructed high-resolution speed fields from aggregated data using signal-reconstruction techniques, while Wang et al. (2023) used Hankel tensor decomposition to capture temporal continuity and impute missing values. These approaches are effective in capturing recurrent patterns, but their accuracy decreases under abrupt traffic condition changes or unreliable sensor measurements. More recently, deep learning has expanded the scope of data-driven TSE. Generative adversarial networks (GANs) have been applied to quantify uncertainty and reconstruct missing traffic states from partial observations (Mo et al., 2022a). Normalizing flows provide flexible probabilistic models for complex traffic state distributions (Huang et al., 2023), while variational autoencoders (VAEs) embed traffic states into low-dimensional latent spaces for imputation and anomaly detection (Boquet et al., 2020). Despite these advances, deep learning models remain difficult to interpret (Shi et al., 2021) and generally require large amounts of representative data to achieve stable performance over regions with long-term missing observations. Beyond these parametric and deep learning approaches, Gaussian process (GP) models provide a nonparametric probabilistic approach to TSE. Several recent works introduce GP priors whose covariance structure reflects macroscopic traffic-flow properties. Yuan et al. (2021) proposed a physics-regularized Gaussian process in which the kernel is constructed such that sampled trajectories remain close to solutions of the kinematic-wave model. Wu et al. (2024) developed anisotropic Gaussian processes with different propagation speeds in free-flow and congested states, capturing the directional nature of traffic waves. GP-based methods offer uncertainty estimates and can incorporate simple forms of traffic physics through kernel design. However, they require relatively dense observations to calibrate kernel hyperparameters, and the resulting uncertainty reflects interpolation error rather than the posterior variability arising from structural sparsity.

Recent work has applied diffusion models to traffic state estimation under different observation settings. Under fully observed or densely observed data, diffusion models have been used to learn spatiotemporal traffic patterns directly. For example, Lei et al. (2024) trained a conditional diffusion model on complete speed fields and then conditioned on partial values to estimate traffic states at uninstrumented locations. Similarly, Lu et al. (2025) introduced a multi-scale diffusion structure that exploits correlations between coarse and fine resolutions to impute missing detector data, assuming that full-resolution targets are available during training. A second set of studies considers heterogeneous sensing environments. Zhang et al. (2025a) proposed a graph-based diffusion framework that integrates loop detectors, probe vehicles, and contextual information, and Lyu and Antoniou (2025) formulated a diffusion-based expectation-maximization strategy to jointly handle noise and missing entries by treating the clean traffic field as a latent variable. These works demonstrate that diffusion priors can capture variability in traffic conditions and can operate with multiple data sources when the training set is sufficiently complete. High-resolution trajectory studies also highlight the importance of dense fields for downstream analysis. For instance, Ji et al. (2026) used nearly complete vehicle trajectories from the I-24 MOTION testbed to quantify stop-and-go wave characteristics. While this line of work does not address reconstruction from sparse loop-probe networks, it underscores the level of detail required for dynamical analysis and further motivates methods capable of recovering such fields from limited observations.

Overall, existing TSE methods show a clear trade-off between using physical models and relying on data. Model-driven approaches are interpretable and work well when the traffic model and its parameters are accurate, but their performance degrades when the assumed model does not match actual traffic conditions. In contrast, data-driven approaches can capture rich spatiotemporal relationships without specifying a traffic model, but they usually rely on densely observed or well-imputed training data and provide limited physical guarantees when observations are sparse or heterogeneous.

2.2. Physics-Informed Deep Learning (PIDL) for TSE

Physics-Informed Deep Learning (PIDL) incorporates traffic-flow theory into neural networks by adding constraints derived from conservation laws or fundamental diagram relations to the training objective (Raissi et al., 2019; Di et al., 2023). In highway traffic state estimation, Huang and Agarwal (2020) applied this idea to first-order LWR and CTM formulations, developed a Physics-Informed Neural Network (PINN) framework based on the LWR conservation law and Greenshields' fundamental diagram. Shi et al. (2021) extended the PINN framework to a second order Aw-Rascle-Zhang (ARZ) model by penalizing continuity and momentum residuals in the loss. Based on these PINN based method, Zhang et al. (2024) represented the discretized traffic flow model as a computational graph and treated fundamental diagram parameters as trainable variables. Wang et al. (2024) developed a stochastic physics-informed model that treats demand and model parameters as random variables, allowing the method to estimate traffic states and parameters together with their uncertainty. For signalized arterial roads, Abewickrema et al. (2026) developed a phase-aware PIDL framework that incorporates conservation constraints and signal-phase information into the loss to estimate traffic state. In parallel, several works have incorporated traffic-flow physics into nonparametric probabilistic models that are not deep networks but play a similar regularizing role (Di et al., 2023). Yuan et al. (2021) proposed a physics-regularized Gaussian process model in which the covariance structure is designed so that sampled trajectories remain close to solutions of a macroscopic kinematic-wave model. Wu et al. (2024) developed anisotropic Gaussian processes whose kernels encode different propagation speeds in free-flow and congested states, effectively embedding kinematic-wave anisotropy into the prior. At the network scale, Xue et al. (2024) designed a graph neural network for traffic state imputation and added penalties that discourage violations of a network macroscopic fundamental diagram, so that the imputed states are consistent with aggregate network flow theory.

These PIDL and physics-regularized methods show that embedding macroscopic flow constraints can improve robustness and interpretability when complete or densely observed traffic states are available, or when density and flow can be reliably reconstructed. However, they also have two important limitations relative to our setting. First, detector layout and observation mask are typically encoded directly in the training loss, tightly coupled to a particular sensor layout and masking pattern. When detector locations or probe penetration rates change at deployment, the training-time loss no longer matches the actual measurement operator, and performance may degrade (Di et al., 2023; Xue et al., 2024). Second, most existing PIDL approaches require access to complete traffic state fields during training. In practice, such complete fields are rarely available, and loop detector and probe vehicle networks provide only sparse and irregular samples. As a result, standard PIDL methods are not appropriate to apply directly in incompletely observed regimes.

2.3. Traffic State Estimation as an Inverse Problem

2.3.1. Inverse problems and the position of TSE

Inverse problems aim to recover an unknown signal or field \mathbf{x} from indirect, noisy measurements \mathbf{y} , typically modeled as $\mathbf{y} = \mathcal{A}(\mathbf{x}) + \boldsymbol{\eta}$, where \mathcal{A} is a known or parametrized forward operator and $\boldsymbol{\eta}$ denotes measurement noise (Tarantola, 2005; Ribes and Schmitt, 2008). Many problems in imaging, geophysics, and remote sensing fit this form and are ill-posed in the sense of non-uniqueness or instability, so meaningful solutions require regularization or Bayesian priors on \mathbf{x} (Barrett and Myers, 2013; Daubechies et al., 2004; Donoho, 2006). A standard distinction is between linear and nonlinear problems, depending on whether \mathcal{A} is linear, and between non-blind and blind formulations, depending on whether the operator and noise statistics are known (Ribes and Schmitt, 2008). From a Bayesian viewpoint, both cases can be written as inference on a posterior density

$$p(\mathbf{x} | \mathbf{y}) \propto p(\mathbf{y} | \mathbf{x}) p(\mathbf{x}), \quad (2.1)$$

where $p(\mathbf{x})$ encodes prior information about the unknown field and $p(\mathbf{y} | \mathbf{x})$ is the likelihood induced by \mathcal{A} and $\boldsymbol{\eta}$.

Classical approaches impose analytic regularizers such as ℓ_2 , ℓ_1 , or total variation penalties and solve the resulting optimization problem (Daubechies et al., 2004; Donoho, 2006). More recent methods use plug-and-play denoisers or regularization-by-denoising strategies, which combine a physics-based forward model with a learned image prior inside an iterative algorithm (Venkatakrishnan et al., 2013; Romano et al., 2017; Kamilov et al., 2023). Deep generative models extend this idea by learning expressive priors $p(\mathbf{x})$ from data and using them within posterior sampling or variational strategies for linear and mildly nonlinear inverse problems (Song and Ermon, 2019; Ho et al., 2020; Kawar et al., 2022; Chung et al., 2023).

Traffic state estimation fits naturally into this framework. In the TSE setting, we let \mathbf{x} denote the full speed field on a discretized highway corridor and let \mathbf{y} collect sparse, noisy measurements from loop detectors, probe vehicles, and camera systems. The observation process can be represented as a linear operator that applies masking, spatial sampling, and local averaging to \mathbf{x} , followed by additive noise. When sensor locations, aggregation intervals, and basic calibration are known, traffic state estimation corresponds to a large-scale, non-blind linear inverse problem with highly structured missing data. If detection rates, outages, or miscalibration are uncertain, the problem becomes semi-blind and more ill-conditioned. As we mentioned in previous subsection, existing traffic state estimation methods usually apply Kalman-type filters, PDE-based reconstruction methods, or deep learning models conditioned on partial observations. These approaches estimate states directly and do not learn a reusable generative prior over full speed fields that can be combined with different observation mask.

In this work, we formulate highway traffic state estimation as a Bayesian inverse problem with an unconditional prior $p_\theta(\mathbf{V})$ over complete speed fields and a likelihood that encodes the mask-structured measurement operator. The prior is learned from historical data and does not depend on a particular detector layout or probe penetration rate. During inference, we combine $p_\theta(\mathbf{V})$ with a masked Gaussian likelihood and a physics-motivated projector inside a diffusion-based sampler. This formulation follows recent developments in diffusion-based inverse problems in imaging, but is adapted to the linear, mask-structured operators and macroscopic flow constraints that arise in highway monitoring (Song et al., 2021; Chung and Ye, 2022; Kawar et al., 2022; Chung et al., 2023). It provides a common framework in which a single prior can be reused under different sensor configurations while physics enters through modular projection rather than through the training loss.

2.3.2. Diffusion models as generative priors for inverse problems and TSE

Diffusion and score-based models learn data distributions by gradually corrupting a clean sample \mathbf{x}_0 with Gaussian noise and training a neural network to approximate the reverse denoising process (Ho et al., 2020; Song et al., 2020). In the variance-preserving setting, the forward corruption at time t has the closed-form expression; a detailed derivation and discussion can be found in Song et al. (2020).

$$\mathbf{x}_t = \sqrt{\alpha(t)} \mathbf{x}_0 + \sqrt{1 - \alpha(t)} \boldsymbol{\epsilon}, \quad \boldsymbol{\epsilon} \sim \mathcal{N}(\mathbf{0}, \mathbf{I}), \quad (2.2)$$

where $\alpha(t)$ is a decreasing function. A neural network $\boldsymbol{\epsilon}_\theta$ is trained to predict the injected noise through the denoising objective

$$\mathcal{L}(\theta) = \mathbb{E}[\|\boldsymbol{\epsilon} - \boldsymbol{\epsilon}_\theta(\mathbf{x}_t, t)\|^2], \quad (2.3)$$

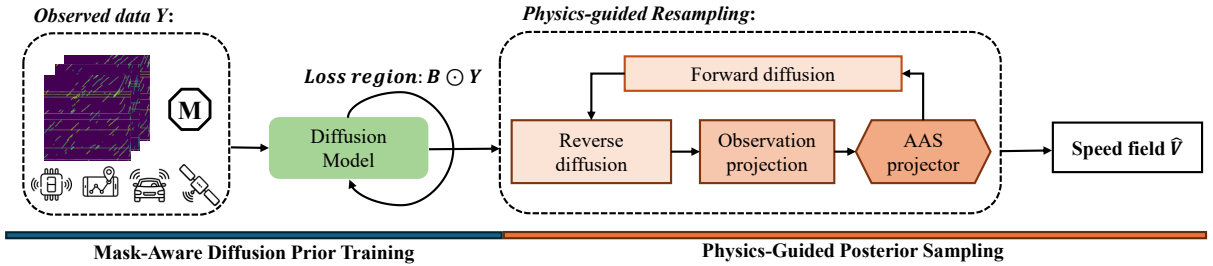


Figure 1: Overall pipeline of the proposed PMA-Diffusion framework.

which provides a score approximation

$$\nabla_{\mathbf{x}_t} \log p_t(\mathbf{x}_t) \approx -\frac{1}{\sigma_t} \varepsilon_\theta(\mathbf{x}_t, t). \quad (2.4)$$

After discretizing the reverse dynamics, the model defines a Markov chain whose stationary distribution approximates the data distribution. The learned model therefore acts as an unconditional prior distribution, $p_\theta(\mathbf{x})$, and sometimes referred to as a *generative prior* or a *diffusion prior*.

Generative priors can be combined with known forward operators to solve inverse problems. A typical solver alternates (i) a reverse-diffusion update, which moves the current iterate toward high-density regions under $p_\theta(\mathbf{x})$, and (ii) a data-consistency step that enforces agreement with the observations. RePaint performs inpainting by interleaving reverse steps with occasional forward re-noising and exact replacement on the observed pixels (Lugmayr et al., 2022). DDRM derives closed-form conditional updates for linear Gaussian operators (Kawar et al., 2022). Diffusion Posterior Sampling (DPS) incorporates likelihood gradients or approximate pseudoinverses to guide sampling for a range of linear problems, including MRI reconstruction (Song et al., 2021; Chung and Ye, 2022; Chung et al., 2023). Recent theoretical work studies these algorithms as approximations to Bayesian posterior sampling in high-dimensional inverse problems.

3. Methodology

In this section, we present the details of PMA-Diffusion. The goal is to reconstruct high-resolution traffic speed fields from sparse and heterogeneous measurements. The method has two main components: a mask-aware diffusion prior and a physics-guided sampling strategy. The first stage aims to train the generative prior $p_\theta(V)$ directly from incomplete observations. After the training stage, we then use the trained diffusion prior in the Physics-Guided posterior sampling stage to inject measurements during the reverse process of the diffusion model through the resampling strategy and enforce traffic constraints through a physics-guided projection operator.

Figure 1 summarizes the overall pipeline of the proposed PMA-Diffusion Framework. The following subsections formalize the problem setting, present the mask-aware diffusion training strategy, and describe the physics-guided sampling procedure.

3.1. Problem Setting

To formalize the reconstruction task, we discretize the highway corridor into S spatial steps and T time steps. Let $V \in [0, 1]^{S \times T}$ denote the latent (noise-free) normalized speed field, obtained by dividing physical speeds by a fixed v_{\max} so that each entry satisfies $V_{s,t} \in [0, 1]$. Only a small fraction of entries are observed; the remainder must be inferred.

3.1.1. Observation measurement

Our observed data come from two asynchronous sources: loop detectors and probe vehicles. Their spatio-temporal coverage is illustrated in Figure 2.

- **Loop detectors.** Loop detectors are fixed-point sensors installed at selected highway segments. Their spatial configuration is time-invariant and is represented by a binary mask $\mathbf{M}^{(\ell)} \in \{0, 1\}^{S \times T}$, where $M_{s,t}^{(\ell)} = 1$ indicates an observed entry. The related observation noise is modeled as $\varepsilon^{(\ell)} \sim \mathcal{N}(0, \sigma_\ell^2 \mathbf{I})$.

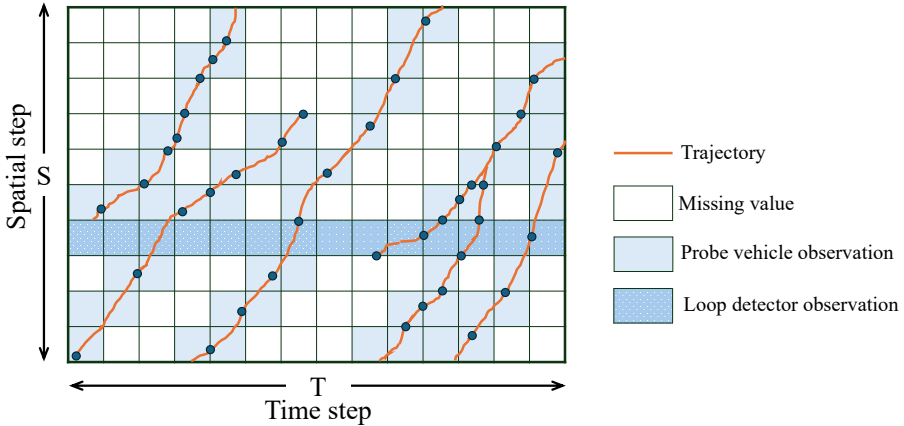


Figure 2: Matrix representation of traffic state variables collected from probe vehicles and loop detectors.

- **Probe vehicles.** Probe vehicle data are generated from moving vehicles equipped with GPS or other communication devices. Unlike loop detectors, probe vehicle data exhibit a stochastic sampling pattern across space and time, represented by $\mathbf{M}^{(p)} \in \{0, 1\}^{S \times T}$. The related observation noise is modeled as $\epsilon^{(p)} \sim \mathcal{N}(0, \sigma_p^2 \mathbf{I})$.

The combined observation mask is defined as $\mathbf{M} = \mathbf{M}^{(\ell)} \vee \mathbf{M}^{(p)}$. In typical highway monitoring scenarios, the visibility ratio is $\rho = \|\mathbf{M}\|_0 / (ST)$, where $\|\mathbf{M}\|_0 = \sum_{s,t} M_{s,t}$ is the number of observed entries, and we typically have $\rho \ll 1$.

Incorporating a possible GPS latency τ , we write the observation operator \mathcal{O}_ρ as

$$\mathcal{O}_\rho(\mathbf{V}) = \mathbf{M}^{(\ell)} \odot (\mathbf{V} + b^{(\ell)} + \epsilon^{(\ell)}) + \mathbf{M}^{(p)} \odot (S_{-\tau} \mathbf{V} + b^{(p)} + \epsilon^{(p)}), \quad (3.1)$$

where \odot denotes the element-wise product, $b^{(\cdot)}$ denotes a sensor-specific bias field, and $S_{-\tau}$ is a shift operator that moves the field backward in time by the GPS latency τ , consistent with Kim and Coifman (2014).

3.1.2. Empirical evidence and assumptions

Recent physics-informed and data-driven TSE studies typically assume that GPS latency (τ) is negligible relative to the aggregation interval, and that low-frequency sensor biases $b^{(\cdot)}$ can be absorbed into the observation noise $\epsilon^{(\cdot)}$ without explicit modeling (Shi et al., 2021; Wu et al., 2024; Wang et al., 2023). We follow the same practice and make the following working assumptions.

Assumption 1 (Negligible latency). *We assume $\tau = 0$, so probe vehicle data are effectively time-aligned with loop detector data.*

Assumption 2 (Bounded low-frequency drift). *The sensor bias field $b^{(\cdot)}$ is L_b -Lipschitz and bounded in amplitude, $\|b^{(\cdot)}\|_\infty \leq \delta$. We absorb $b^{(\cdot)}$ into the noise term, which introduces at most $O(\delta)$ bias in the score used for training.*

Remark 1. Consider the (single-source) conditional log-likelihood,

$$\log p(Y | V) = \log p_\eta(Y - V - b^{(\cdot)}). \quad (3.2)$$

If $b^{(\cdot)}$ is Lipschitz-continuous and small in amplitude, a first-order Taylor expansion around $b^{(\cdot)} = 0$ gives

$$\log p_\eta(Y - V - b^{(\cdot)}) = \log p_\eta(Y - V) - \nabla_y \log p_\eta(Y - V)^T b^{(\cdot)} + O(\delta^2). \quad (3.3)$$

Differentiating with respect to V shows that the score is perturbed by at most $O(\delta)$ when we replace $(Y - V - b^{(\cdot)})$ with $(Y - V)$. This motivates treating the masked score estimator as approximately unbiased when δ is small.

Under Assumptions 1-2, the observation model in Eq. (3.1) simplifies to

$$\mathbf{Y} = \mathbf{M}^{(\ell)} \odot (\mathbf{V} + \epsilon^{(\ell)}) + \mathbf{M}^{(p)} \odot (\mathbf{V} + \epsilon^{(p)}). \quad (3.4)$$

To make the subsequent masking analysis clear, we impose the following additional assumptions.

Assumption 3 (Noise conditional independence). *Given the latent speed field \mathbf{V} , the loop detector and probe vehicle noise fields are independent: $\epsilon^{(\ell)} \perp\!\!\!\perp \epsilon^{(p)} \mid \mathbf{V}$.*

Assumption 4 (Missing-at-random masking). *Conditioned on \mathbf{V} , the masking process is independent of the observation noise:*

$$\mathbf{M}^{(\cdot)} \perp\!\!\!\perp \epsilon^{(\cdot)} \mid \mathbf{V}.$$

Under these working assumptions, we can write the observation model in a compact form as

$$\mathbf{Y} = \mathbf{M} \odot (\mathbf{V} + \epsilon), \quad \epsilon \sim \mathcal{N}(0, \sigma^2 \mathbf{I}). \quad (3.5)$$

3.1.3. Bayesian posterior perspective

Given \mathbf{Y} and \mathbf{M} , our goal is to draw samples from the posterior distribution

$$p(\mathbf{V} \mid \mathbf{Y}) \propto \underbrace{\mathbf{1}[\mathbf{V} \in \mathcal{P}_{\text{phys}}]}_{\text{physics surrogate}} \times \underbrace{p_{\theta}(\mathbf{V})}_{\text{mask-aware diffusion prior}} \times \underbrace{\exp\left[-\frac{1}{2\sigma^2} \|\mathbf{(V} \odot \mathbf{M}) - \mathbf{Y}\|_F^2\right]}_{\text{masked likelihood}}, \quad (3.6)$$

where $\mathcal{P}_{\text{phys}}$ is the physics surrogate restricts \mathbf{V} to fields that satisfy the physics constraint. $p_{\theta}(\mathbf{V})$ is the mask-aware prior learned from historical data. The masked likelihood incorporates the measurements only at the observed entries specified by \mathbf{M} . Together, these terms define the distribution of all speed fields that are physically reasonable, consistent with historical data, and match the available observations.

Remark 2. *Bayes' rule factorizes the posterior as*

$$p(\mathbf{V} \mid \mathbf{Y}) \propto p(\mathbf{V}) \cdot p(\mathbf{Y} \mid \mathbf{V}). \quad (3.7)$$

Because the noise acts only on visible pixels, the likelihood becomes

$$p(\mathbf{Y} \mid \mathbf{V}) = \prod_{(s,t): M_{s,t}=1} \frac{1}{\sqrt{2\pi} \sigma} \exp\left[-\frac{(Y_{s,t} - V_{s,t})^2}{2\sigma^2}\right], \quad (3.8)$$

which is exactly the exponential term in Eq. (3.6). The likelihood depends only on the measurements on the support of \mathbf{M} and leaves unobserved entries unconstrained. The prior $p_{\theta}(\mathbf{V})$ introduces data-driven regularization, and the indicator $\mathbf{1}[\mathbf{V} \in \mathcal{P}_{\text{phys}}]$ restricts the support to speed fields that satisfy the surrogate physics constraints.

To sample from Eq. (3.6), we introduce a mask-aware diffusion prior training strategy in Section 3.2 and a physics-guided sampling strategy in Section 3.3 that alternates reverse diffusion, observation projection, and physics projection.

3.2. Mask-Aware Diffusion Prior

To learn the data-driven prior $p_{\theta}(\mathbf{V})$ that appears in the Bayesian posterior (Eq. 3.6), we must train a generative model directly from the same sparsely observed speed fields available at inference. However, classical denoising-diffusion probabilistic models (DDPMs, Ho et al. (2020)) require fully observed training data. This condition is rarely satisfied in highway traffic state estimation, where each speed field $\mathbf{V} \in \mathbb{R}^{S \times T}$ is only partially revealed through a binary mask \mathbf{M} . If such incomplete observations are treated as inputs, the learned prior may fail to capture the true variability in unobserved regions. To overcome this mismatch, we employ an Ambient Diffusion (Daras et al., 2023) strategy, which integrates the masking process directly into the data distribution.

Specifically, during training we draw $\tilde{\mathbf{M}} \sim \pi(\mathbf{M}_0)$ from the same law expected at inference, combining fixed loop detector positions with randomly sampled probe trajectories. Here, π denotes the empirical distribution of masks observed in the raw data. The partially observed input is then constructed as

$$\mathbf{Y}_0 = \tilde{\mathbf{M}} \odot (\mathbf{V} + \epsilon). \quad (3.9)$$

The denoiser is conditioned on the current mask $\tilde{\mathbf{M}}$, so its prediction uses the observed values while recognizing which entries are missing. Under Assumptions 3 and 4, the masked denoising objective corresponds to learning the conditional score on the unobserved entries given the observed ones, even though a full \mathbf{V} is never available. This allows the sensing sparsity to be incorporated directly into the learned prior without relying on external preprocessing or imputation.

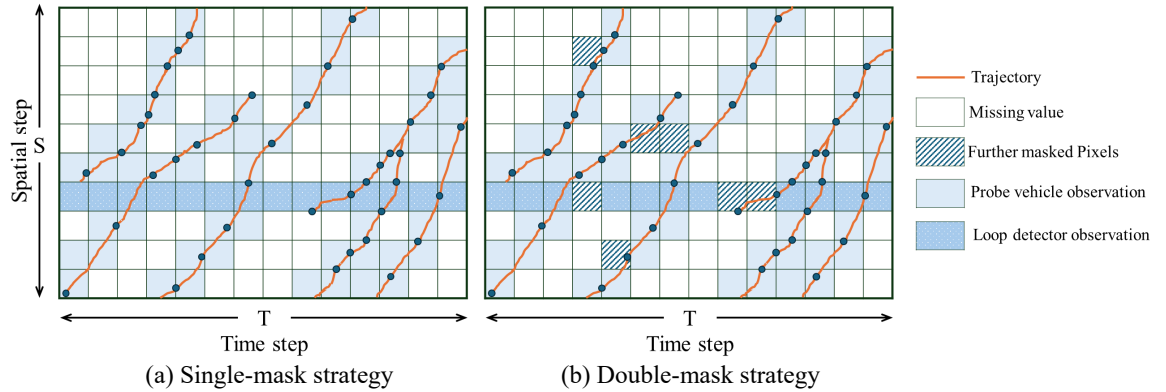


Figure 3: Illustration of two mask strategy. Left: original observed data under the single-mask strategy, reflecting actual sparse sensor coverage. Right: the same frame with further masked pixels, simulating the observation pattern under the double-mask strategy.

3.2.1. Mask-selection strategies

Observation masks are heterogeneous: some pixels (e.g., near fixed detectors) are almost always visible, while others remain persistently hidden. To account for this, we consider two complementary training strategies summarized in Table 1.

In the single mask strategy, the true sensor mask \mathbf{M} is left untouched; the network is therefore penalized only on truly known pixels. This works well when probe vehicle coverage is dense and roughly random. Under such conditions every spatial-temporal position is observed at least occasionally. In the double-mask strategy, when the overall visibility ratio $\rho = \|\mathbf{M}\|_0/(ST)$ is high, we draw the auxiliary mask \mathbf{B} from the empirical mask distribution $\pi(\mathbf{M})$ captured in the raw data. When ρ is low, we instead sample \mathbf{B} from a Bernoulli distribution with parameter p_{extra} , so that every coordinate is occasionally masked and therefore contributes to the loss. In practice we use $p_{\text{extra}} = 0.05$, which improves interpolation near fixed loop locations while incurring negligible additional variance, see Figure 3.

3.2.2. *Mask-aware training process*

To construct a mask-aware prior, we explicitly mimic the sensing sparsity during training. For each speed field \mathbf{V} we first sample a training mask $\tilde{\mathbf{M}}$ (according to the single- or double-mask strategy) and build

$$\mathbf{Y}_0 = C_\rho(\mathbf{V}) = \tilde{\mathbf{M}}_{s,t} \odot (\mathbf{V} + \boldsymbol{\varepsilon}), \quad (3.10)$$

where $\tilde{\mathbf{M}}_{s,t} = 1$ marks an observed pixel, C_ρ denotes the masking operator with the ratio ρ . Next we corrupt \mathbf{Y}_0 with Gaussian noise first before asking the network to denoise it.

Step 1 - Forward corruption (variance-preserving SDE). We gradually add Gaussian noise to \mathbf{Y}_0 using the variance-preserving SDE

$$d\mathbf{Y}_t = -\frac{1}{2} \beta(t) \mathbf{Y}_t dt + \sqrt{\beta(t)} d\mathbf{W}_t, \quad \beta(t) = \beta_0 + (\beta_1 - \beta_0)t, \quad (3.11)$$

where W_t is a standard Wiener process. Then the closed-form solution for $t \in [0, 1]$ is

$$\mathbf{Y}_t = \sqrt{\alpha(t)} \mathbf{Y}_0 + \sqrt{1 - \alpha(t)} \boldsymbol{\eta}, \quad \boldsymbol{\eta} \sim \mathcal{N}(\mathbf{0}, \mathbf{I}), \quad \alpha(t) = \exp\left(-\int_0^t \beta(s) \, ds\right). \quad (3.12)$$

Table 1

Table 1
Mask-selection strategies for training the diffusion prior.

Strategy	Pixels kept	Regions contributing to loss	When to prefer
Single mask	$\mathbf{M}_{s,t} = 1$	\mathbf{M}	All pixels have non-zero probability of being observed.
Double mask	$\mathbf{M}_{s,t} = 1$	$\tilde{\mathbf{M}} = \mathbf{B} \odot \mathbf{M}$	Some pixels are always invisible (e.g. fixed loop detectors)

Thus, as t increases, $\alpha(t)$ decreases; and the further the diffusion proceeds, the closer \mathbf{Y}_t becomes to pure noise.

Step 2 - Masked score matching (noise prediction). Given $(\mathbf{Y}_t, t, \mathbf{M})$, the denoiser $h_\theta(\cdot)$ is trained to predict the injected noise $\boldsymbol{\eta}$, but only where we have data:

$$\mathcal{L}(\theta) = \mathbb{E}[\lambda(t) \|\mathbf{M} \odot (h_\theta(\mathbf{Y}_t, t, \mathbf{M}) - \boldsymbol{\eta})\|_F^2], \quad \lambda(t) = \alpha(t)/(1 - \alpha(t)). \quad (3.13)$$

Here $\lambda(t)$ re-weights time steps according to the signal-to-noise ratio, and the Frobenius norm $\|\cdot\|_F$ sums squared errors over $\mathbf{M}_{s,t} = 1$. Under the standard noise-prediction parameterization (Daras et al., 2023), the conditional score for unobserved pixels ($\mathbf{M}_{s,t} = 0$) is approximated by

$$\nabla_{\mathbf{Y}_t} \log p_t(\mathbf{Y}_t) \approx -\frac{1}{\sigma_t} h_\theta(\mathbf{Y}_t, t, \mathbf{M}), \quad (3.14)$$

and Assumption 4 ensures that the loss in Eq. (3.13) matches the corresponding masked score-matching objective. We therefore view h_θ as a data-driven approximation of the conditional score under the same masking law that will be encountered at inference time.

Overall, the procedure creates a stochastic corruption-restoration process: we corrupt a sparsely observed speed field with noise (forward SDE) and train the network to reverse that corruption (masked score matching). Unlike imputation-based pre-processing, which risks propagating bias from heuristic gap-filling, the proposed strategy trains the prior directly from incomplete observations. As a result, the diffusion prior $p_\theta(\mathbf{V})$ captures the spatiotemporal dynamics of traffic speeds without requiring fully observed training data.

3.3. Physics-Guided Posterior Sampler

While the learned diffusion prior p_θ effectively captures the distribution of highway speed fields, it is agnostic to two essential constraints: (i) strict fidelity to partial observations (\mathbf{Y}, \mathbf{M}) and (ii) consistency with macroscopic traffic-flow principles. Naively conditioning on observations through noise replacement or direct imputation often leads to sharp discontinuities and physically implausible structures in the reconstructed regions, particularly under severe sparsity. Conversely, exact enforcement of conservation laws is infeasible in the present setting, where only normalized speeds are observed and neither density nor flow can be reliably recovered. To address this gap, we introduce a surrogate physics posterior that integrates three complementary elements: a data-driven prior, exact observation fidelity, and a soft projection toward physically reasonable patterns. In practice, we implement this idea through a physics-guided posterior sampler. We view the resulting sampling strategy as a heuristic algorithm for approximately exploring the surrogate posterior in Eq. (3.6), rather than as an exact Markov chain Monte Carlo method, and we do not claim theoretical convergence to the target distribution.

3.3.1. Surrogate physics posterior

Let $p_\theta(\mathbf{V})$ denote the mask-aware diffusion prior. Our target distribution for inference is the surrogate physics posterior, see Eq. 3.6. Let $\mathcal{P}_{\text{phys}} \subset [0, 1]^{S \times T}$ denotes a surrogate physics set, implicitly defined by a mask-invariant projection operator

$$\mathcal{P}_{\text{phys}} : \underbrace{[0, 1]^{S \times T}}_{\text{current speed field } \mathbf{V}} \times \underbrace{\{0, 1\}^{S \times T}}_{\text{mask } \mathbf{M}} \xrightarrow{P_{\text{phys}}} \underbrace{[0, 1]^{S \times T}}_{\text{updated field}}. \quad (3.15)$$

Here, we approximate it through an outer constrained reverse process that alternates reverse-diffusion updates with observation and physics projections while incorporating a physics-guided projector.

3.3.2. Physics-guided posterior sampler

At each reverse-diffusion iteration, the sampler alternates three operations: (i) **Denoise**: Use the denoiser to draw the current sample one step closer to the learned prior, (ii) **Observation projection**: Replace every visible pixel with its exact measurement to preserve data fidelity, and (iii) **Physics projection**: Project the missing pixels onto the low-frequency manifold $\mathcal{P}_{\text{phys}}$ defined by the traffic surrogate. An optional forward jump re-injects a small amount of forward noise, then resumes the reverse process.

In our setting, we draw $\mathbf{Z}_T \sim \mathcal{N}(\mathbf{0}, \mathbf{I})$ with a linear β -schedule of length $T = 500$. For $t = T-1, \dots, 0$, perform:

$$\text{Reverse diffusion: } \tilde{\mathbf{Z}}_t = g_\theta(\mathbf{Z}_{t+1}, t+1), \quad (3.16)$$

$$\text{Observation projection: } \hat{\mathbf{Z}}_t = P_{\text{obs}}(\tilde{\mathbf{Z}}_t) = \mathbf{Y} \odot \mathbf{M} + \tilde{\mathbf{Z}}_t \odot (1 - \mathbf{M}), \quad (3.17)$$

$$\text{Physics projection: } \bar{\mathbf{Z}}_t = P_{\text{phys}}(\hat{\mathbf{Z}}_t, \mathbf{M}), \quad (3.18)$$

$$\text{Optional forward jump: } \mathbf{Z}_t = f_j(\bar{\mathbf{Z}}_t, t) = \sqrt{\frac{\alpha(t)}{\alpha(t+j)}} \bar{\mathbf{Z}}_t + \sqrt{1 - \frac{\alpha(t)}{\alpha(t+j)}} \epsilon. \quad (3.19)$$

where \mathbf{Z}_t denotes the sampler state at reverse step t , g_θ denotes the reverse diffusion kernel, and f_j denotes the forward jump operator. The observation projection (3.17) ensures exact data fidelity on $\mathbf{M} = 1$, while the physics projector (3.18) acts only on the missing subspace, enforcing mask-invariance:

$$P_{\text{phys}}(\mathbf{V}, \mathbf{M}) \odot \mathbf{M} = \mathbf{V} \odot \mathbf{M}. \quad (3.20)$$

Repeating this constrained loop yields $\{\mathbf{Z}_0^{(n)}\}_{n=1}^N$, an approximate ensemble of posterior samples for uncertainty quantification.

3.3.3. Physics-guided projector.

The current instantiation of P_{phys} employs an Adaptive Anisotropic Smoothing (AAS) operator, which extends the Generalized Adaptive Smoothing Method (GASM) (Treiber et al., 2011) into a mask-aware and diffusion compatible form. Unlike full conservation enforcement, which is infeasible under speed-only observations, AAS acts as a local regularizer that promotes physically plausible structures in unobserved regions while preserving exact fidelity on measured pixels, see Algorithm 1. Its design is guided by three principles:

1. **Characteristic coherence.** Anisotropic smoothing aligns kernel support with admissible forward/backward slopes $c \in \{c_{\text{free}}, c_{\text{cong}}\}$ (after conversion by $\Delta t / \Delta x$), approximating propagation along traffic waves instead of isotropic blurring.
2. **Soft regime transition:** Instead of a hard free-flow or congestion split, AAS introduces a differentiable gate $p_{\text{free}} = \frac{1}{2}(1 + \tanh((V_{s,t} - v_{\text{thr}})/\beta))$ that blends the free-flow and congested kernels.
3. **Bounded first-order transport residual:** A residual term $R_{s,t} = (V_{s,t} - V_{s,t-1}) + c_{s,t}(V_{s,t} - V_{s-1,t})$ penalizes local violations of the first-order kinematic wave relation $\partial_t V + c \partial_x V \approx 0$, providing a lightweight consistency proxy without requiring explicit density or flow estimates.

The resulting update is applied only on $(1 - \mathbf{M})$:

$$V^{(1)} = V - \alpha_{\text{smooth}}(V - V_s) \odot (1 - \mathbf{M}), \quad V^{(2)} = V^{(1)} - \alpha_{\text{char}} R \odot (1 - \mathbf{M}), \quad (3.21)$$

where V_s is the blended anisotropic surrogate field and $\alpha_{\text{smooth}} \gg \alpha_{\text{char}}$ ensures numerical stability. A final clipping step projects the result onto $[0, 1]$. By construction, the update is mask-invariant and acts only on the missing subspace, and the step sizes $(\alpha_{\text{smooth}}, \alpha_{\text{char}})$ are chosen so that the projector remains numerically stable under iterative application within the diffusion loop.

The physics-guided posterior sampler combines the generative prior with a physics projector that enforces basic traffic-flow structure on the missing region. A central design feature is modularity: any projector that is (i) mask-invariant, (ii) non-expansive on the missing subspace, and (iii) computationally local can replace or augment AAS without retraining the prior p_θ . The same interface also allows multiple physics modules to be applied in sequence. If additional variables such as density, flow, or ramp counts become available, projectors based on conservation relations or fundamental-diagram consistency (e.g., P_{cons} , P_{FD}) can be inserted into the sampling loop. In the current speed-only setting we use only P_{AAS} , but the framework accommodates richer physics when appropriate data are available.

4. Experimental Evaluation

We conduct a comprehensive empirical evaluation to assess the effectiveness of **PMA-Diffusion**. The experiments are structured around two central research questions, each aligned with one stage in the PMA-Diffusion framework:

RQ1 – Prior learning: How well a diffusion prior can be learned on incomplete speed fields?

Algorithm 1 AAS Projector: Physics-guided Mask-invariant Projection

Require: Speed field $V \in [0, 1]^{S \times T}$; mask $\mathbf{M} \in \{0, 1\}^{S \times T}$; physical parameters $(v_{\text{thr}}, \beta, c_{\text{free}}^{\text{phys}}, c_{\text{cong}}^{\text{phys}})$; smoothing weights $(\alpha_{\text{smooth}}, \alpha_{\text{char}})$; kernel stds $(\sigma_{\text{par}}, \sigma_t)$.

Ensure: Updated field $P_{\text{phys}}(V, \mathbf{M})$.

- 1: Compute soft regime gate:
$$p_{\text{free}} \leftarrow 0.5(1 + \tanh((V - v_{\text{thr}})/\beta))$$
- 2: Convert characteristic speeds to grid units: $c_{\text{free}} \leftarrow c_{\text{free}}^{\text{phys}} \Delta t / \Delta x$; $c_{\text{cong}} \leftarrow c_{\text{cong}}^{\text{phys}} \Delta t / \Delta x$
- 3: Build two anisotropic Gaussian kernels $K_{c_{\text{free}}}, K_{c_{\text{cong}}}$ aligned with slopes $c_{\text{free}}, c_{\text{cong}}$ (normalized).
- 4: Apply separable convolution: $V_f \leftarrow K_{c_{\text{free}}} * V$, $V_c \leftarrow K_{c_{\text{cong}}} * V$
- 5: Compute blended surrogate: $V_s \leftarrow p_{\text{free}} \odot V_f + (1 - p_{\text{free}}) \odot V_c$
- 6: **Step 1 (smooth relax):** $V^{(1)} \leftarrow V - \alpha_{\text{smooth}}(V - V_s) \odot (1 - \mathbf{M})$
- 7: **if** transport correction enabled **then**

 - 8: Compute local speed $c_{\text{loc}} \leftarrow p_{\text{free}} c_{\text{free}} + (1 - p_{\text{free}}) c_{\text{cong}}$
 - 9: Compute residual: $R \leftarrow (V_{s,t}^{(1)} - V_{s,t-1}^{(1)}) + c_{\text{loc}}(V_{s,t}^{(1)} - V_{s-1,t}^{(1)})$
 - 10: **Step 2 (residual update):** $V^{(2)} \leftarrow V^{(1)} - \alpha_{\text{char}} R \odot (1 - \mathbf{M})$

- 11: **else**
- 12: $V^{(2)} \leftarrow V^{(1)}$
- 13: **end if**
- 14: Clip to valid range: $V^{(2)} \leftarrow \text{clip}(V^{(2)}, 0, 1)$
- 15: **return** $P_{\text{phys}}(V, \mathbf{M}) = V^{(2)}$

RQ2 – Posterior sampling: Given a fixed prior, how much the sampling stage can recover under varying sensing sparsity?

PMA-Diffusion consists of two main components: (i) a mask-aware diffusion prior trained directly from sparsely observed speed fields, and (ii) a physics-guided posterior sampler that alternates reverse-diffusion updates, observation projection, and physics-guided projection. **RQ1** evaluates whether a diffusion prior trained under sparse supervision (Single-mask and Double-mask training strategies) can approach the performance of a model trained on fully observed speed fields. **RQ2** then examines how much the proposed posterior sampler can further improve reconstruction accuracy by enforcing data fidelity and basic kinematic-wave structure under different sensing sparsity levels.

4.1. Dataset, Pre-processing, Experimental Set-up

The study corridor corresponds to the Tennessee Department of Transportation's I-24 Mobility Technology Interstate Observation Network (I-24 MOTION; Gloudemans et al. (2023)) data. I-24 MOTION data are captured by 276 pole-mounted high-resolution traffic cameras that provide seamless coverage of approximately 4.2 miles along the I-24 highway corridor near Nashville, TN. In our experiment, we convert vehicle trajectories into lane-level speed fields on a fixed Eulerian grid with $S = 200$ spatial pixels ($\Delta x = 100\text{ft}$), four lanes, and $T = 200$ time slices ($\Delta t = 1\text{s}$), so that each sample spans approximately 3.8 miles over 200 seconds. Figure 4 shows randomly selected samples from the dataset. The dataset is split into 70% / 10% / 20% for training, validation, and testing, respectively. and all quantitative evaluations are conducted on test samples.

The I-24 MOTION offers two advantages for this study. First, its near-complete spatial and temporal coverage yields a "ground-truth" speed field, which allows us to mask the data synthetically and evaluate reconstruction error at every hidden pixel. Second, it includes dense and clean vehicle trajectories that capture real traffic movements without the gaps and noise found in typical probe vehicle data. By sub-sampling I-24 MOTION to mimic realistic detector layouts and probe vehicle trajectories, we can test PMA-Diffusion under controlled sparsity levels while still comparing the results against a fully observed baseline.

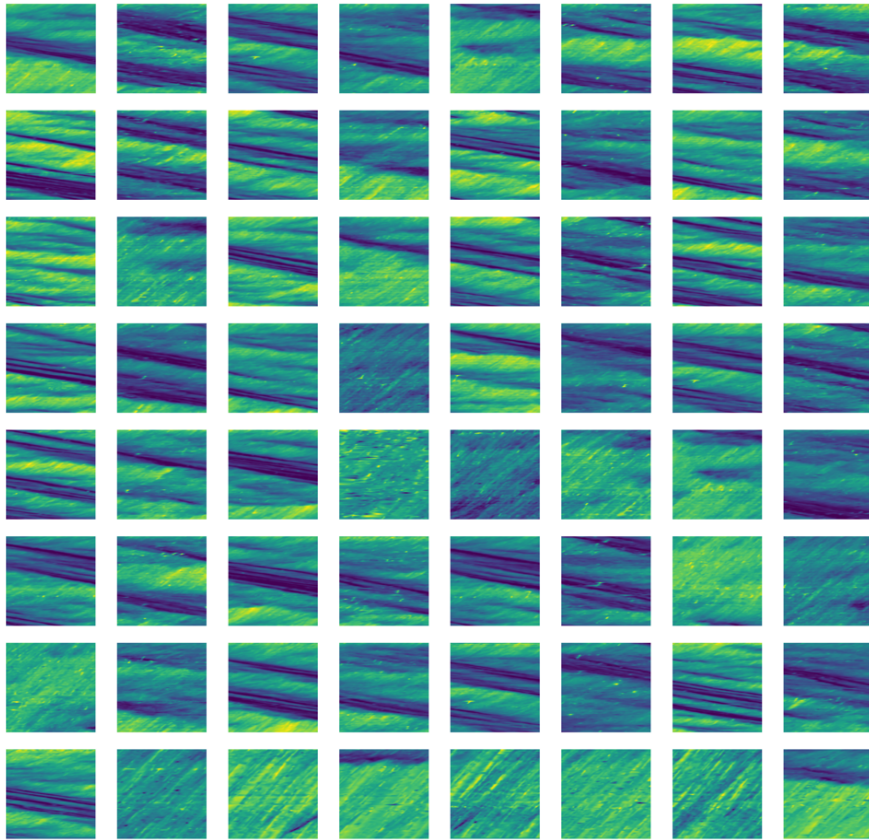


Figure 4: Random speed field samples from I-24 MOTION dataset. These samples illustrate the spatial-temporal structure (propagating waves, lane heterogeneity) that the model is required to learn.

4.1.1. Observation models

We collect synthetic observation (\mathbf{Y}) and mask (\mathbf{M}) pairs based on the ground-truth speed field (\mathbf{V}) to simulate the real-world scenarios. Our masks have two components:

- **Loop detectors mask:** In practice, the Loop detectors are fixed in a specific location. We generate a fixed Loop detector mask $\mathbf{M}^{(l)}$ and mask 5%, 15%, 25% of the row data as observed data $\mathbf{M}^{(l)} \odot \mathbf{V}$.
- **Probe vehicles mask:** To simulate probe vehicle data, we use real I-24 MOTION trajectories to build observation masks. We randomly select a subset of vehicle IDs from the preprocessed data and reconstruct their trajectories using position, timestamp, and speed information. In the experiments, we evaluate four probe density levels, corresponding to $\lambda = 0, 5, 15$, and 25, respectively.

Building on Assumption 1 and Assumption 2, we resample the probe vehicle trajectories directly onto the Eulerian grid. This ensures that the probe vehicle observations align with the grid and removes small misalignment effects. Figure 5 shows the ground-truth speed field and the three corresponding observation masks: (b) the loop detector mask, (c) the probe vehicle mask obtained from resampled trajectories, and (d) the total observed mask formed by their union.

4.2. Evaluation Metrics

We evaluate reconstruction quality only on the unobserved pixels, because the observed pixels are directly replaced by measurements during sampling and therefore do not indicate how well the model can recover missing states. Meanwhile, our goal is not to assess point-wise prediction accuracy, but to measure whether the generated speed fields are reasonable, physically plausible, and consistent with macroscopic traffic patterns. Following Choi et al. (2025), we use three complementary metrics.

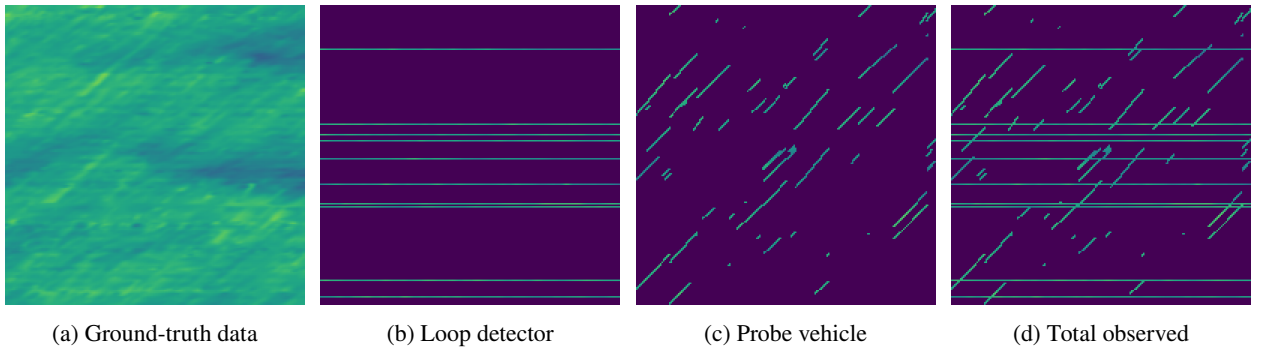


Figure 5: Observation Patterns from Loop detectors and Probe vehicles. Dark areas denote unobserved pixels; colored entries denote observed speeds.

1. **Masked-MSE (2×2).** We first apply a 2×2 average pooling to both the reconstruction and the ground truth, and then compute the mean squared error on the unobserved pixels. This metric measures the accuracy of the low-frequency component of the speed field, which is most relevant for traffic operations, such as identifying the onset and extent of congestion, and for computing link travel times. The pooling step reduces sensitivity to very local differences (e.g., a one-pixel shift of a wave front) that are less important at the macroscopic level.
2. **Sobel-MSE.** We apply a Sobel operator to extract spatial and temporal gradients of the speed field, and then compute the mean squared error between the edge maps of the reconstruction and the ground truth on the unobserved pixels. This metric emphasizes the reconstruction of high-frequency structures, in particular the location and sharpness of stop-and-go waves and shock fronts, which are central to many traffic-flow analyses.
3. **LPIPS.** We report the Learned Perceptual Image Patch Similarity (LPIPS) score with an AlexNet backbone (Zhang et al., 2018) on the unobserved pixels. LPIPS compares feature representations in a pretrained network and serves as a perceptual measure of similarity between two spatiotemporal speed fields. It captures differences in pattern shape and texture that may not be fully reflected in pixel-wise errors but matter for visual inspection and qualitative traffic pattern analysis.

4.3. Models

The three training and sampling strategies introduced below are structured specifically to isolate the contributions of the prior and the sampling mechanism with respect to RQ1 and RQ2, respectively.

4.3.1. Training strategy

We evaluate three training strategies designed to isolate the effects of supervision.

- **Full-obs** The network trained by fully latent speed field data \mathbf{V} ; the value of **Full-obs** represents the upper bound, showing how well the DDPM architecture alone can fit fully observed data.
- **Single-mask** Each training sample is corrupted by its own visibility mask, exactly mirroring realistic loop detectors + probe vehicles coverage. The model therefore learns only from genuinely observed pixels.
- **Double-mask** On top of the true visibility map we apply an additional mask (see Table 1). Hiding even "always visible" rows encourages the network to reason about persistently unseen locations and improves robustness when some pixels are never measured in practice.

All three variants share the same UNet backbone, which is the most widely used backbone neural network structure for diffusion models (Ronneberger et al., 2015; Ho et al., 2020). Specifically, our UNet backbone is configured with one input channel, 48 base feature channels, four resolution levels with channel multipliers of (1, 2, 4, 8) and 4-head linear attention in the bottleneck. We use a linear β -schedule with $T=500$ steps from $\beta_0 = 10^{-4}$ to $\beta_T = 2 \times 10^{-2}$ and optimize the Huber loss ($\delta = 1$), which is numerically more stable than ℓ_2 . We train for 50 epochs using Adam ($\text{lr} = 5 \times 10^{-4}$, batch size = 64). The model training time is around 300 minutes of GPU time. All experiments are

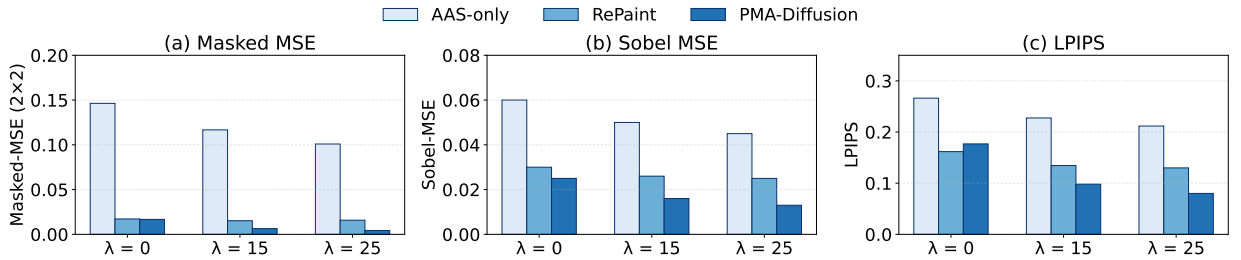


Figure 6: Performance of different samplers based on Full-obs model (row = 5%).

conducted on a shared GPU server equipped with two AMD EPYC Milan 7643 CPUs, four NVIDIA RTX 6000 Ada Generation GPUs with 48 GB GDDR6 memory, 1 TB system memory, and NVMe storage. In this study we only use a single NVIDIA RTX 6000 Ada GPU for training and inference.

4.3.2. Sampling strategy

Using the diffusion prior from the training stage, we compare two main diffusion based sampling strategies and one physics-only baseline.

1. **AAS-only baseline.** We start from the partially observed field \mathbf{Y} and apply the AAS projector for a number of iterations. At each iteration, the observed pixels (mask $M = 1$) are kept unchanged, and the projector updates only the missing pixels ($M = 0$) by anisotropic smoothing and a small first-order correction. This baseline does not use the diffusion model.
2. **RePaint.** We follow the RePaint inpainting strategy: the sampler alternates reverse-diffusion steps with occasional small forward noising steps, while repeatedly resetting the observed pixels to their measurements to better satisfy the observation mask.
3. **PMA-Diffusion.** We start from the same inpainting strategy and, after enforcing the observations, apply the AAS projector on the unobserved pixels, so that the missing region is guided toward simple first-order traffic patterns without changing the observed data.

The β -schedule and timestep ($T=500$) are shared with training stage. RePaint uses the same U-Net to predict ϵ_θ ; the physics projector is parameter-free at test time once the hyper-parameters are fixed.

4.4. Experimental Results

Tables 2 report LPIPS, Masked-MSE, and Sobel-MSE across all combinations of training mode, observation density (row-mask: 5% \rightarrow 25%), probe intensity ($\lambda : 0 \rightarrow 25$), and sampler (AAS-only, RePaint, PMA-Diffusion). To interpret these results, it is useful to recall how visibility is defined across different models. In the **Full-obs model** (M1), the network is trained on fully observed (ground-truth) speed fields, and the row visibility and λ values apply only at sampling stage. In contrast, the **Single-mask** (M2) and **Double-mask** (M3) models are both trained and evaluated under the same partial-observation condition. Thus, for M2 and M3, the specified row and λ values reflect the entire modeling pipeline, not only the inference stage.

We organize the discussion in three steps. First, we fix the training strategy to the Full-obs model and compare the three sampling strategies to assess the value of the proposed PMA-Diffusion sampler. Second, we fix the sampler to PMA-Diffusion and compare the three training strategies to evaluate how close mask-aware training can get to the Full-obs upper bound. Finally, we summarize the overall trends and additional analyses.

4.4.1. Effect of sampling strategies under a fully observed prior

We first consider the Full-obs prior (M1), which is trained on fully observed speed fields and therefore represents the best-case scenario for the diffusion architecture itself. This setting isolates the effect of the sampling strategy, since differences cannot be attributed to missing data during training.

Figure 6 shows Masked-MSE, Sobel MSE, and LPIPS for the three samplers under the sparse setting with 5% fixed rows and no probe vehicles. In this case, the AAS already achieves a Masked-MSE of 0.1463 on the unobserved pixels.

RePaint further reduces the error to 0.0172 by iteratively mixing forward and reverse steps. Adding the physics projector (PMA-Diffusion) yields a slight additional reduction in Masked-MSE and improves Sobel-MSE, indicating better alignment of wave fronts.

Across the other row and λ combinations for M1 in Table 2, the same pattern holds. AAS sampling provides a reasonable baseline. RePaint consistently improves both Masked-MSE and LPIPS by exploiting iterative resampling. The proposed PMA-Diffusion sampler, which augments RePaint with the AAS projector, either matches or improves on RePaint in almost all settings and is particularly effective at reducing Sobel-MSE in sparse configurations. This confirms that, when the prior is well-trained, the PMA-Diffusion sampler gives the best overall reconstruction quality among the three options.

4.4.2. Effect of training strategies under the PMA-Diffusion sampler

Based on the comparison above, we fix the sampler to PMA-Diffusion and compare the three training strategies: Full-obs (M1), Single-mask (M2), and Double-mask (M3). This addresses RQ1 by asking how much accuracy is lost when the prior is trained only on incomplete fields, and to what extent the proposed double-mask strategy can close the gap to the Full-obs upper bound.

Table 2

Quantitative comparison of three training modes (M1: Full-obs, M2: Single-mask, M3: Double-mask) on 200×200 grids under different row coverage levels (Row) and probe intensities (λ). For each setting we report LPIPS, Masked-MSE (2×2), and Sobel-MSE for three reconstruction methods (AAS-only, RePaint, PMA-Diffusion). All metrics are computed on unobserved pixels; lower values indicate better reconstruction.

Mode	Row	λ	LPIPS			Masked-MSE (2×2)			Sobel-MSE		
			AAS-only	RePaint	PMA	AAS-only	RePaint	PMA	AAS-only	RePaint	PMA
M1	5%	0	0.2662	0.1617	0.1768	0.1463	0.0172	0.0167	0.0028	0.0013	0.0009
		5	0.2466	0.1491	0.1357	0.1356	0.0155	0.0113	0.0030	0.0014	0.0008
		15	0.2275	0.1345	0.0981	0.1167	0.0152	0.0064	0.0033	0.0017	0.0008
		25	0.2117	0.1299	0.0800	0.1009	0.0158	0.0043	0.0034	0.0019	0.0008
	15%	0	0.1187	0.0823	0.0381	0.0523	0.0195	0.0018	0.0043	0.0038	0.0006
		5	0.1179	0.0854	0.0353	0.0487	0.0185	0.0017	0.0042	0.0037	0.0006
		15	0.1169	0.0908	0.0311	0.0421	0.0165	0.0016	0.0039	0.0035	0.0006
		25	0.1140	0.0936	0.0294	0.0367	0.0146	0.0014	0.0036	0.0033	0.0006
	25%	0	0.0821	0.0657	0.0322	0.0416	0.0104	0.0018	0.0032	0.0022	0.0006
		5	0.0848	0.0701	0.0300	0.0387	0.0099	0.0017	0.0031	0.0022	0.0006
		15	0.0843	0.0769	0.0266	0.0336	0.0089	0.0015	0.0029	0.0022	0.0006
		25	0.0836	0.0828	0.0253	0.0294	0.0083	0.0014	0.0027	0.0022	0.0006
M2	5%	0	0.2662	0.8455	0.1851	0.1463	7.1959	0.0364	0.0028	0.3112	0.0008
		5	0.2466	0.3540	0.1406	0.1356	0.1727	0.0133	0.0030	0.0116	0.0008
		15	0.2275	0.4048	0.0981	0.1167	0.1105	0.0052	0.0033	0.0058	0.0008
		25	0.2117	0.1966	0.0821	0.1009	0.0199	0.0042	0.0034	0.0029	0.0008
	15%	0	0.1187	1.2911	0.0367	0.0523	2.8315	0.0018	0.0043	5.1773	0.0006
		5	0.1179	0.2089	0.0373	0.0487	0.3862	0.0018	0.0042	0.0751	0.0006
		15	0.1169	0.1301	0.0310	0.0421	0.0826	0.0014	0.0039	0.0135	0.0006
		25	0.1140	0.1615	0.0288	0.0367	0.1069	0.0013	0.0036	0.0179	0.0006
	25%	0	0.0821	0.2347	0.0315	0.0416	0.2279	0.0017	0.0032	0.2615	0.0006
		5	0.0848	0.1377	0.0301	0.0387	0.1153	0.0016	0.0031	0.0202	0.0006
		15	0.0843	0.1583	0.0265	0.0336	0.1214	0.0014	0.0029	0.0208	0.0006
		25	0.0836	0.1691	0.0246	0.0294	0.1170	0.0012	0.0027	0.0210	0.0005
M3	5%	0	0.2662	0.4920	0.1833	0.1463	0.2962	0.0289	0.0028	0.2066	0.0008
		5	0.2466	0.1579	0.1352	0.1356	0.0697	0.0124	0.0030	0.0035	0.0008
		15	0.2275	0.1171	0.0980	0.1167	0.0420	0.0071	0.0033	0.0028	0.0008
		25	0.2117	0.1049	0.0789	0.1009	0.0487	0.0039	0.0034	0.0030	0.0008
	15%	0	0.1187	0.2082	0.0372	0.0523	0.2389	0.0017	0.0043	0.3609	0.0006
		5	0.1179	0.1511	0.0347	0.0487	0.1607	0.0016	0.0042	0.0242	0.0006
		15	0.1169	0.1404	0.0305	0.0421	0.1103	0.0014	0.0039	0.0220	0.0006
		25	0.1140	0.1466	0.0289	0.0367	0.0948	0.0013	0.0036	0.0173	0.0006
	25%	0	0.0821	0.2008	0.0316	0.0416	0.1948	0.0017	0.0032	0.3363	0.0006
		5	0.0848	0.1888	0.0296	0.0387	0.1965	0.0016	0.0031	0.0331	0.0006
		15	0.0843	0.1616	0.0264	0.0336	0.1274	0.0014	0.0029	0.0254	0.0006
		25	0.0836	0.1861	0.0245	0.0294	0.1309	0.0013	0.0027	0.0245	0.0006

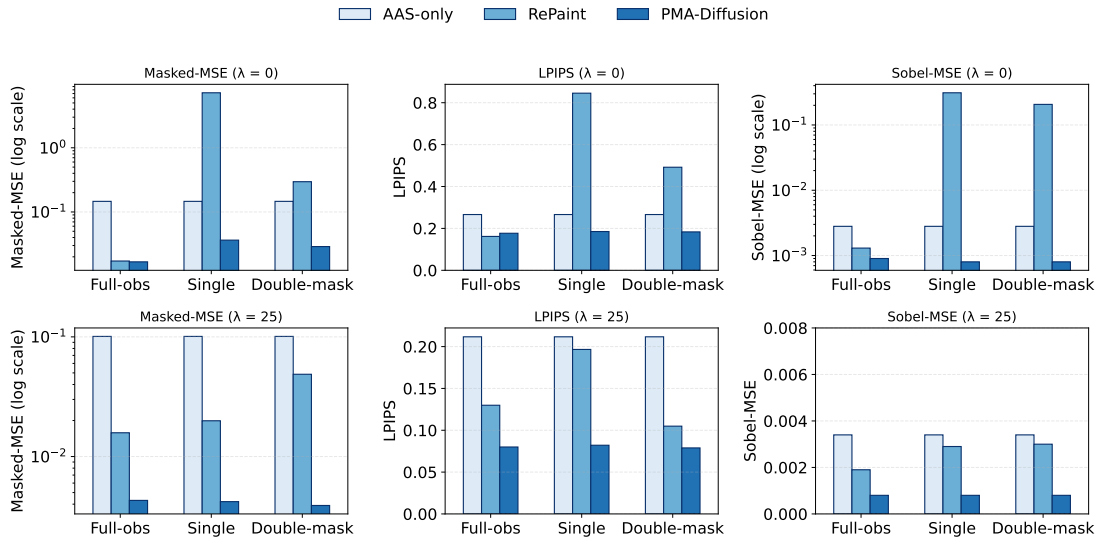


Figure 7: Quantitative comparison of Masked-MSE, LPIPS, and Sobel-MSE across three training modes (Full-obs, Single-mask, Double-mask) under Row = 5% for two probe intensities, $\lambda = 0$ and $\lambda = 25$.

Under the most challenging setting with 5% rows and $\lambda = 0$, the differences between the three training strategies are clear. With PMA-Diffusion sampling, the Full-obs model achieves a Masked-MSE of 0.0167, while the Single-mask model reaches 0.0364 and the Double-mask model reaches 0.0289 (Table 2). In the same setting, LPIPS follows the same ordering, and Sobel-MSE remains at the 10^{-3} level for all three, showing that all models can reproduce wave structures but differ in low-frequency accuracy. Figure 7 summarizes Masked-MSE trends across λ for the most sparse row setting.

The Single-mask prior suffers whenever parts of the grid are rarely or never visible during training. In this regime, the RePaint samplers can be unstable: for example, with 5% rows and $\lambda = 0$, the RePaint sampler yields a Masked-MSE above 7 and a LPIPS of 0.8455 for M2, reflecting severe over-extrapolation in unobserved regions. Once PMA-Diffusion is used, these pathologies are largely corrected and the error drops by several orders of magnitude, but the gap to the Full-obs prior remains noticeable.

The Double-mask prior (M3) substantially improves robustness while using the same underlying dataset as M2. By randomly hiding additional pixels during training, it forces the model to learn to interpolate across persistently unseen regions. As a result, under 5% rows and $\lambda = 0$, the Double-mask model with PMA-Diffusion reduces Masked-MSE from 0.0364 (M2) to 0.0289 (M3), and in many denser settings the gap to the Full-obs prior becomes small. For example, for 15% rows and $\lambda = 15$, the Full-obs model with PMA-Diffusion has Masked-MSE 0.0016, while the Double-mask counterpart achieves 0.0014. In some dense states (e.g., 25% rows and $\lambda = 25$), the Single-mask and Double-mask models with PMA-Diffusion both approach the Full-obs baseline and can slightly outperform each other depending on the metric, suggesting that when every pixel is frequently observed in historical data, Single-mask training is sufficient.

Under the PMA-Diffusion sampler, the proposed Double-mask training strategy close most of the gap to the Full-obs upper bound, especially in sparse states. Single-mask training strategy can approach the Full-obs performance only when each location is observed with sufficient frequency in the training data. Also, physics guidance through the AAS projector maintains performance across all configurations in Table 2. It either leaves the metrics unchanged or improves them. The gain is most significant under sparse observations (e.g., 5% rows), where the projector stabilizes the unobserved regions.

4.4.3. Qualitative illustration

Figure 8 compares the PMA-Diffusion reconstruction against the ground truth using the Double-mask model under both low-observation (row = 15%, $\lambda = 15$) and high-observation (row = 25%, $\lambda = 25$) settings. While the generated speed field appears smoother and exhibits slight discontinuities between generated and observed regions, its overall

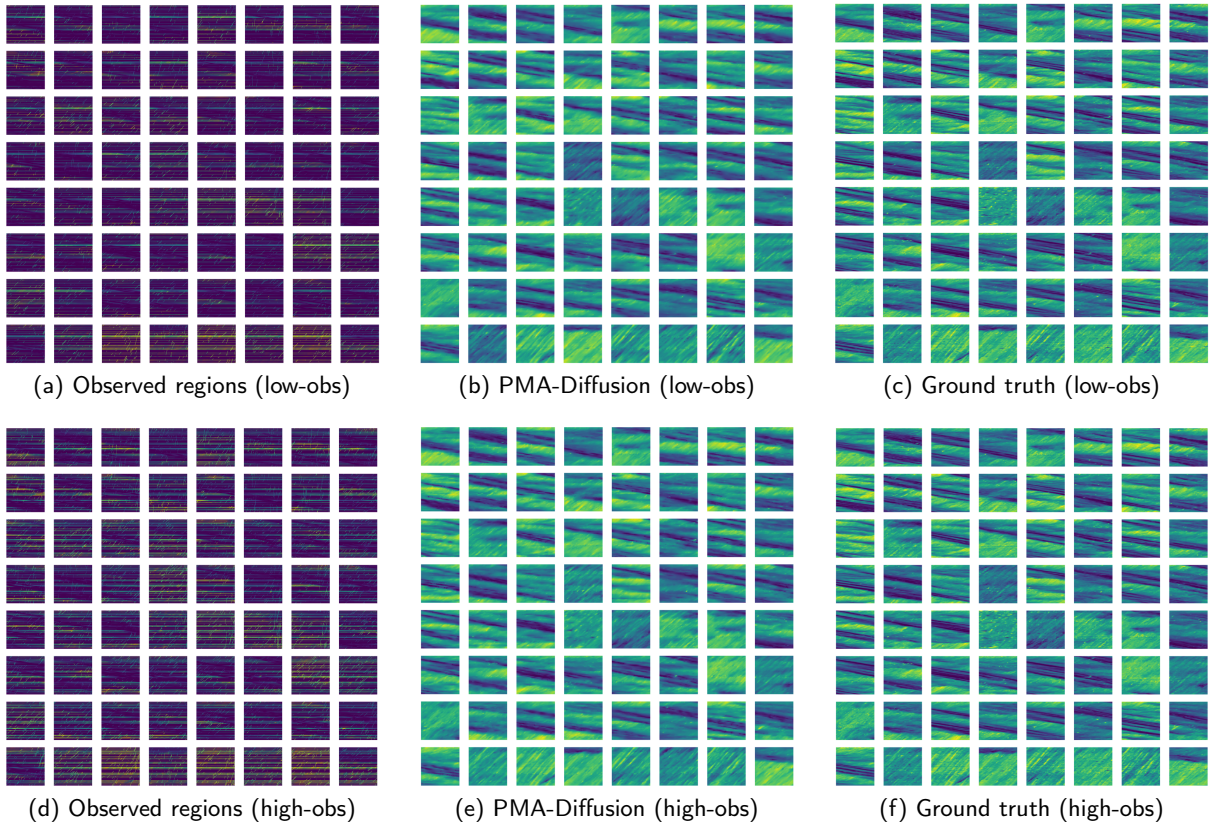


Figure 8: Visual comparison between Observed regions, PMA-Diffusion, and Ground truth under the Double-mask model for low-observation (row = 15%, $\lambda = 15$) and high-observation (row = 25%, $\lambda = 25$) scenarios.

Table 3

Quantitative results for the double-mask model (M3) on 64x64 grids under different row coverage levels (Row) and probe intensities (λ). For each setting, we report LPIPS, Masked-MSE (2x2), and Sobel-MSE for three reconstruction methods (AAS-only, RePaint, and PMA-Diffusion). All metrics are computed on unobserved pixels, and lower values indicate better reconstruction quality.

Mode	Row	λ	LPIPS			Masked-MSE (2x2)			Sobel-MSE		
			AAS-only	RePaint	PMA	AAS-only	RePaint	PMA	AAS-only	RePaint	PMA
Double-mask model (M3)	5%	0	0.2333	0.9164	0.0719	0.4122	0.2194	0.0120	0.0013	0.5189	0.0009
		5	0.1776	0.0479	0.0124	0.2706	0.1184	0.0032	0.0012	0.0017	0.0009
		15	0.0863	0.0388	0.0050	0.1306	0.0541	0.0020	0.0010	0.0019	0.0008
		25	0.0536	0.0676	0.0035	0.0746	0.0957	0.0018	0.0009	0.0039	0.0007
	15%	0	0.0388	0.3976	0.0032	0.0808	1.4737	0.0018	0.0014	1.6367	0.0008
		5	0.0340	0.0323	0.0030	0.0548	0.0609	0.0017	0.0011	0.0053	0.0007
		15	0.0232	0.0278	0.0026	0.0283	0.0238	0.0016	0.0008	0.0013	0.0007
		25	0.0147	0.0219	0.0024	0.0171	0.0158	0.0015	0.0006	0.0010	0.0005
	25%	0	0.0399	0.2450	0.0032	0.0745	1.6512	0.0017	0.0007	0.1234	0.0007
		5	0.0325	0.0606	0.0028	0.0496	0.2309	0.0016	0.0007	0.0086	0.0006
		15	0.0226	0.0408	0.0026	0.0262	0.0598	0.0014	0.0006	0.0021	0.0006

spatiotemporal structure remains consistent and physically coherent. This suggests that the model effectively captures macroscopic traffic patterns, even if some high-frequency details are attenuated during sampling.

4.4.4. Performance across different Spatial-Temporal Resolutions

To examine scalability and resolution sensitivity, we re-discretize the same I-24 dataset from 200x200 grids ($\Delta t=1$ s, $\Delta x=100$ ft) to 64x64 grids ($\Delta t=5$ s, $\Delta x=200$ ft), while strictly preserving the spatiotemporal domain and

visibility patterns. Under the 64×64 setting, we use the same model family and training protocol: a UNet with one input channel and 64 base feature channels, three resolution levels with channel multipliers (1, 2, 4), and 4-head linear attention in the bottleneck; a linear β -schedule with $T=500$ steps ($\beta_0=10^{-4}$, $\beta_T=2 \times 10^{-2}$); Huber loss ($\delta=1$); and Adam (learning rate 5×10^{-4} , batch size = 250). Training runs for 10 epochs (approximately 1.8×10^3 iterations), requiring about 15 minutes of GPU time. During inference, we apply the same four sampling methods as in the high-resolution setting.

The results show that the trends observed at 64×64 are consistent with those at 200×200 , and are numerically even more stable. PMA-Diffusion achieves the best performance across the majority of configurations. For example, under the Double-mask (M3) setting with $\text{Row} = 15\%$ and $\lambda = 15$, the Masked-MSE decreases from 0.0238 (RePaint) to 0.0016 after applying AAS. Correspondingly, LPIPS improves from 0.0278 to 0.0026, and Sobel-MSE improves from 0.0013 to 0.0007.

In the most sparse setting ($\text{Row} = 5\%$, $\lambda = 0$), both the Single-mask and Double-mask priors can exhibit instability or over-extrapolation when using RePaint, whereas PMA-Diffusion reduces Masked-MSE to 0.0120 (M3), representing an order-of-magnitude improvement over RePaint (0.2194). Even in the Full-obs model (M1), PMA-Diffusion achieves a Masked-MSE of 0.0013 at $\text{Row} = 25\%$, $\lambda = 25$, indicating that posterior refinement guided by physics remains beneficial even when the prior is already strong. For brevity, Table 3 reports representative configurations on 64×64 grids.

5. Conclusion

This paper presents **PMA-Diffusion**, a physics-guided, mask-aware diffusion framework for highway traffic state estimation from sparse loop detector and probe vehicle data. The framework reconstructs unobserved speed fields from incomplete observations by combining a diffusion prior with a physics-guided posterior sampler. The prior is trained directly on incompletely observed speed fields using two masking strategies: a single-mask strategy that follows the actual sensor coverage, and a double-mask strategy that adds an auxiliary mask to temporarily hide always-visible pixels. At inference, the sampler alternates reverse-diffusion updates, an observation projection that enforces data fidelity on the visible entries, and a physics-guided projector based on adaptive anisotropic smoothing that enforces the missing region toward kinematic-wave structure.

The study addresses two main questions: How well a diffusion prior can be learned on incomplete speed fields, and given a fixed prior, how much the sampling stage can recover under varying sensing sparsity. The experiments on the I-24 MOTION data show that a mask-aware diffusion prior trained with the double-mask strategy closes most of the gap to a fully supervised model, especially when some pixels are rarely or never observed. Even under severe sparsity (e.g., 5% visibility), the combination of a mask-aware prior and the physics-guided sampler substantially improves reconstruction quality compared with both baselines, and achieves near-full-observation accuracy in several denser settings. These results indicate that PMA-Diffusion provides a practical way to learn reusable high-resolution traffic speed priors from incomplete data and to adapt them to different sensing layouts through our physics-guided posterior sampler.

Several assumptions made in this study limit the current model. Probe vehicle and loop detector data are treated as time-aligned (Assumption 1), and low-frequency sensor bias is assumed to be small and smooth enough to be absorbed into Gaussian noise (Assumption 2), leading to the simplified observation model in Eq. (3.4). In addition, the current physics projector acts only on speeds and does not explicitly incorporate other traffic-flow constraints.

Future work can relax these assumptions and better account for heterogeneous data sources. One direction is to develop diffusion training and sampling schemes that model modality-specific noise and bias for loop detectors and probe vehicles, rather than absorbing all differences into a single Gaussian term. This includes handling non-negligible latency, sensor drift and non-Gaussian noise, and possible miscalibration, and examining how these factors affect the diffusion prior and posterior sampling. Another direction is to extend the physics module beyond adaptive anisotropic smoothing. The same projection interface can integrate additional traffic-flow constraints, such as conservation laws, fundamental-diagram consistency, or network-level macroscopic structure.

Declaration of AI and AI-assisted technologies in the writing process

During the preparation of this work, the authors used AI-assisted language polishing tools for language assistance. After utilizing these tools, the authors thoroughly reviewed and revised the content as necessary and take full responsibility for the final version of the published article.

Acknowledgement

We acknowledge the CSE Data Science Initiative at the University of Minnesota College of Science and Engineering for funding through the ADC Graduate Assistantship.

CRediT authorship contribution statement

Lindong Liu: Conceptualization, Data curation, Formal analysis, Investigation, Methodology, Software, Validation, Visualization, Writing – original draft. **Zhixiong Jin:** Conceptualization of this study, Validation Writing - review and editing. **Seongjin Choi:** Conceptualization, Data curation, Formal analysis, Funding acquisition, Investigation, Methodology, Project administration, Supervision, Writing – original draft, Writing – review & editing.

References

Abewickrema, W., Yildirimoglu, M., Kim, J., 2026. A physics-informed deep learning framework for traffic state estimation in signalized arterial roads. *Transportation Research Part C: Emerging Technologies* 182, 105420.

Ahmed, A., Naqvi, S.A.A., Watling, D., Ngoduy, D., 2019. Real-time dynamic traffic control based on traffic-state estimation. *Transportation research record* 2673, 584–595.

Ahmed, A., Ngoduy, D., Watling, D., 2016. Prediction of traveller information and route choice based on real-time estimated traffic state. *Transportmetrica B: Transport Dynamics* 4, 23–47.

Barmpounakis, E., Geroliminis, N., 2020. On the new era of urban traffic monitoring with massive drone data: The pneuma large-scale field experiment. *Transportation research part C: emerging technologies* 111, 50–71.

Barrett, H.H., Myers, K.J., 2013. Foundations of image science. John Wiley & Sons.

Belletti, F., Haziza, D., Gomes, G., Bayen, A.M., 2017. Expert level control of ramp metering based on multi-task deep reinforcement learning. *IEEE Transactions on Intelligent Transportation Systems* 19, 1198–1207.

Boquet, G., Morell, A., Serrano, J., Vicario, J.L., 2020. A variational autoencoder solution for road traffic forecasting systems: Missing data imputation, dimension reduction, model selection and anomaly detection. *Transportation Research Part C: Emerging Technologies* 115, 102622.

Butilă, E.V., Boboc, R.G., 2022. Urban traffic monitoring and analysis using unmanned aerial vehicles (uavs): A systematic literature review. *Remote Sensing* 14, 620.

Choi, S., Jin, Z., Ham, S.W., Kim, J., Sun, L., 2025. A gentle introduction and tutorial on deep generative models in transportation research. *Transportation Research Part C: Emerging Technologies* 176, 105145.

Chung, H., Kim, J., Mccann, M.T., Klasky, M.L., Ye, J.C., 2023. Diffusion posterior sampling for general noisy inverse problems, 2024. URL <https://arxiv.org/abs/2209.14687>.

Chung, H., Ye, J.C., 2022. Score-based diffusion models for accelerated mri. *Medical image analysis* 80, 102479.

Chung, H., Ye, J.C., 2024. Deep diffusion image prior for efficient ood adaptation in 3d inverse problems, in: *European Conference on Computer Vision*, Springer, pp. 432–455.

Coifman, B., 2002. Estimating travel times and vehicle trajectories on freeways using dual loop detectors. *Transportation Research Part A: Policy and Practice* 36, 351–364.

Coric, V., Djuric, N., Vucetic, S., 2012. Traffic state estimation from aggregated measurements with signal reconstruction techniques. *Transportation research record* 2315, 121–130.

Coursey, A., Ji, J., Zhang, Z., Barbour, W., Quinones-Grueiro, M., Derr, T., Biswas, G., Work, D.B., 2025. Real-time freeway traffic anomalous event detection system via radar detector sensors, in: *Proceedings of the ACM/IEEE 16th International Conference on Cyber-Physical Systems (with CPS-IoT Week 2025)*, pp. 1–2.

Daganzo, C.F., 1995. The cell transmission model, part ii: network traffic. *Transportation Research Part B: Methodological* 29, 79–93.

Dasas, G., Shah, K., Dagan, Y., Gollakota, A., Dimakis, A., Klivans, A., 2023. Ambient diffusion: Learning clean distributions from corrupted data. *Advances in Neural Information Processing Systems* 36, 288–313.

Daubechies, I., Defrise, M., De Mol, C., 2004. An iterative thresholding algorithm for linear inverse problems with a sparsity constraint. *Communications on Pure and Applied Mathematics: A Journal Issued by the Courant Institute of Mathematical Sciences* 57, 1413–1457.

Di, X., Shi, R., Mo, Z., Fu, Y., 2023. Physics-informed deep learning for traffic state estimation: A survey and the outlook. *Algorithms* 16, 305.

Donoho, D.L., 2006. Compressed sensing. *IEEE Transactions on information theory* 52, 1289–1306.

Fonod, R., Cho, H., Yeo, H., Geroliminis, N., 2025. Advanced computer vision for extracting georeferenced vehicle trajectories from drone imagery. *Transportation Research Part C: Emerging Technologies* 178, 105205.

Gloudemans, D., Wang, Y., Ji, J., Zachar, G., Barbour, W., Hall, E., Cebelak, M., Smith, L., Work, D.B., 2023. I-24 motion: An instrument for freeway traffic science. *Transportation Research Part C: Emerging Technologies* 155, 104311.

Herrera, J.C., Work, D.B., Herring, R., Ban, X.J., Jacobson, Q., Bayen, A.M., 2010. Evaluation of traffic data obtained via gps-enabled mobile phones: The mobile century field experiment. *Transportation Research Part C: Emerging Technologies* 18, 568–583.

Ho, J., Jain, A., Abbeel, P., 2020. Denoising diffusion probabilistic models. *Advances in neural information processing systems* 33, 6840–6851.

Huang, A.J., Agarwal, S., 2020. Physics informed deep learning for traffic state estimation, in: 2020 IEEE 23rd International Conference on Intelligent Transportation Systems (ITSC), IEEE. pp. 1–6.

Huang, A.J., Agarwal, S., 2022. Physics-informed deep learning for traffic state estimation: Illustrations with lwr and ctm models. *IEEE Open Journal of Intelligent Transportation Systems* 3, 503–518.

Huang, H., Yu, J., Chen, J., Lai, R., 2023. Bridging mean-field games and normalizing flows with trajectory regularization. *Journal of Computational Physics* 487, 112155.

Ji, J., Gloudemans, D., Wang, Y., Zachár, G., Barbour, W., Sprinkle, J., Piccoli, B., Work, D.B., 2026. Scalable analysis of stop-and-go waves: Representation, measurements and insights. *Transportation Research Part C: Emerging Technologies* .

Kamilov, U.S., Bouman, C.A., Buzzard, G.T., Wohlberg, B., 2023. Plug-and-play methods for integrating physical and learned models in computational imaging: Theory, algorithms, and applications. *IEEE Signal Processing Magazine* 40, 85–97.

Kawar, B., Elad, M., Ermon, S., Song, J., 2022. Denoising diffusion restoration models. *Advances in neural information processing systems* 35, 23593–23606.

Kim, S., Coifman, B., 2014. Comparing inrix speed data against concurrent loop detector stations over several months. *Transportation Research Part C: Emerging Technologies* 49, 59–72.

Lei, D., Xu, M., Wang, S., 2024. A conditional diffusion model for probabilistic estimation of traffic states at sensor-free locations. *Transportation Research Part C: Emerging Technologies* 166, 104798.

Liebig, T., Piatkowski, N., Bockermann, C., Morik, K., 2017. Dynamic route planning with real-time traffic predictions. *Information Systems* 64, 258–265.

Lighthill, M.J., Whitham, G.B., 1955. On kinematic waves ii. a theory of traffic flow on long crowded roads. *Proceedings of the royal society of london. series a. mathematical and physical sciences* 229, 317–345.

Liu, H.X., Recker, W., Chen, A., 2004. Uncovering the contribution of travel time reliability to dynamic route choice using real-time loop data. *Transportation Research Part A: Policy and Practice* 38, 435–453.

Liu, J., Barreau, M., Čišić, M., Johansson, K.H., 2021. Learning-based traffic state reconstruction using probe vehicles. *IFAC-PapersOnLine* 54, 87–92.

Liu, Y., Lai, X., Chang, G.L., 2006. Detector placement strategies for freeway travel time estimation, in: 2006 IEEE Intelligent Transportation Systems Conference, IEEE. pp. 499–504.

Lu, B., Miao, Q., Liu, Y., Tamir, T.S., Zhao, H., Zhang, X., Lv, Y., Wang, F.Y., 2025. A diffusion model for traffic data imputation. *IEEE/CAA Journal of Automatica Sinica* 12, 606–617.

Lugmayr, A., Danelljan, M., Romero, A., Yu, F., Timofte, R., Van Gool, L., 2022. Repaint: Inpainting using denoising diffusion probabilistic models, in: Proceedings of the IEEE/CVF conference on computer vision and pattern recognition, pp. 11461–11471.

Lyu, C., Antoniou, C., 2025. A diffusion-based expectation-maximization framework for probabilistic traffic data imputation. *IEEE Internet of Things Journal* .

Mihaylova, L., Boel, R., Hegyi, A., 2006. An unscented kalman filter for freeway traffic estimation. *IFAC Proceedings Volumes* 39, 31–36.

Minnesota Department of Transportation, 2019. Traffic Detection Systems Engineering. MnDOT.

Mo, Z., Fu, Y., Di, X., 2022a. Quantifying uncertainty in traffic state estimation using generative adversarial networks, in: 2022 IEEE 25th International Conference on Intelligent Transportation Systems (ITSC), IEEE. pp. 2769–2774.

Mo, Z., Fu, Y., Xu, D., Di, X., 2022b. Trafficflowgan: Physics-informed flow based generative adversarial network for uncertainty quantification, in: Joint European conference on machine learning and knowledge discovery in databases, Springer. pp. 323–339.

Mori, U., Mendiburu, A., Álvarez, M., Lozano, J.A., 2015. A review of travel time estimation and forecasting for advanced traveller information systems. *Transportmetrica A: Transport Science* 11, 119–157.

Ni, D., Leonard, J.D., 2005. Markov chain monte carlo multiple imputation using bayesian networks for incomplete intelligent transportation systems data. *Transportation research record* 1935, 57–67.

Papageorgiou, M., Blosseville, J.M., Haj-Salem, H., 1990. Modelling and real-time control of traffic flow on the southern part of boulevard périphérique in paris: Part ii: Coordinated on-ramp metering. *Transportation Research Part A: General* 24, 361–370.

Raissi, M., Perdikaris, P., Karniadakis, G.E., 2019. Physics-informed neural networks: A deep learning framework for solving forward and inverse problems involving nonlinear partial differential equations. *Journal of Computational physics* 378, 686–707.

Rempe, F., Franeck, P., Bogenberger, K., 2022. On the estimation of traffic speeds with deep convolutional neural networks given probe data. *Transportation research part C: emerging technologies* 134, 103448.

Ribes, A., Schmitt, F., 2008. Linear inverse problems in imaging. *IEEE Signal Processing Magazine* 25, 84–99.

Richards, P.I., 1956. Shock waves on the highway. *Operations research* 4, 42–51.

Romano, Y., Elad, M., Milanfar, P., 2017. The little engine that could: Regularization by denoising (red). *SIAM journal on imaging sciences* 10, 1804–1844.

Ronneberger, O., Fischer, P., Brox, T., 2015. U-net: Convolutional networks for biomedical image segmentation, in: International Conference on Medical image computing and computer-assisted intervention, Springer. pp. 234–241.

Seo, T., Bayen, A.M., Kusakabe, T., Asakura, Y., 2017. Traffic state estimation on highway: A comprehensive survey. *Annual reviews in control* 43, 128–151.

Seo, T., Kusakabe, T., 2015. Probe vehicle-based traffic state estimation method with spacing information and conservation law. *Transportation Research Part C: Emerging Technologies* 59, 391–403.

Shi, R., Mo, Z., Di, X., 2021. Physics-informed deep learning for traffic state estimation: A hybrid paradigm informed by second-order traffic models, in: Proceedings of the AAAI Conference on Artificial Intelligence, pp. 540–547.

Shi, Z., Chen, Y., Liu, J., Fan, D., Liang, C., 2023. Physics-informed spatiotemporal learning framework for urban traffic state estimation. *Journal of Transportation Engineering, Part A: Systems* 149, 04023056.

Song, Y., Ermon, S., 2019. Generative modeling by estimating gradients of the data distribution. *Advances in neural information processing systems* 32.

Song, Y., Shen, L., Xing, L., Ermon, S., 2021. Solving inverse problems in medical imaging with score-based generative models. *arXiv preprint arXiv:2111.08005*.

Song, Y., Sohl-Dickstein, J., Kingma, D.P., Kumar, A., Ermon, S., Poole, B., 2020. Score-based generative modeling through stochastic differential equations. *arXiv preprint arXiv:2011.13456*.

Storm, P.J., Mandjes, M., van Arem, B., 2022. Efficient evaluation of stochastic traffic flow models using gaussian process approximation. *Transportation research part B: methodological* 164, 126–144.

Tak, S., Woo, S., Yeo, H., 2016. Data-driven imputation method for traffic data in sectional units of road links. *IEEE Transactions on Intelligent Transportation Systems* 17, 1762–1771.

Tarantola, A., 2005. Inverse problem theory and methods for model parameter estimation. SIAM.

Thodi, B.T., Khan, Z.S., Jabari, S.E., Menendez, M., 2022. Incorporating kinematic wave theory into a deep learning method for high-resolution traffic speed estimation. *IEEE transactions on intelligent transportation systems* 23, 17849–17862.

Treibler, M., Helbing, D., 2002. Reconstructing the spatio-temporal traffic dynamics from stationary detector data. *Cooper@tive Tr@nsport@tion Dyn@mics* 1, 3–1.

Treibler, M., Helbing, D., 2003. An adaptive smoothing method for traffic state identification from incomplete information, in: *Interface and transport dynamics: Computational Modelling*. Springer, pp. 343–360.

Treibler, M., Kesting, A., Wilson, R.E., 2011. Reconstructing the traffic state by fusion of heterogeneous data. *Computer-Aided Civil and Infrastructure Engineering* 26, 408–419.

Venkatakrishnan, S.V., Bouman, C.A., Wohlberg, B., 2013. Plug-and-play priors for model based reconstruction, in: *2013 IEEE global conference on signal and information processing*, IEEE, pp. 945–948.

Wang, T., Li, Y., Cheng, R., Zou, G., Dantsujic, T., Ngoduy, D., 2024. Knowledge-data fusion oriented traffic state estimation: A stochastic physics-informed deep learning approach. *arXiv preprint arXiv:2409.00644*.

Wang, X., Wu, Y., Zhuang, D., Sun, L., 2023. Low-rank hankel tensor completion for traffic speed estimation. *IEEE Transactions on Intelligent Transportation Systems* 24, 4862–4871.

Wang, Y., Papageorgiou, M., 2005. Real-time freeway traffic state estimation based on extended kalman filter: a general approach. *Transportation Research Part B: Methodological* 39, 141–167.

Work, D.B., Tossavainen, O.P., Blandin, S., Bayen, A.M., Iwuchukwu, T., Tracton, K., 2008. An ensemble kalman filtering approach to highway traffic estimation using gps enabled mobile devices, in: *2008 47th IEEE Conference on Decision and Control*, IEEE, pp. 5062–5068.

Wu, F., Cheng, Z., Chen, H., Qiu, Z., Sun, L., 2024. Traffic state estimation from vehicle trajectories with anisotropic gaussian processes. *Transportation Research Part C: Emerging Technologies* 163, 104646.

Xue, J., Ka, E., Feng, Y., Ukkusuri, S.V., 2024. Network macroscopic fundamental diagram-informed graph learning for traffic state imputation. *Transportation Research Part B: Methodological* 189, 102996.

Yin, W., Murray-Tuite, P., Rakha, H., 2012. Imputing erroneous data of single-station loop detectors for nonincident conditions: Comparison between temporal and spatial methods. *Journal of Intelligent Transportation Systems* 16, 159–176.

Yuan, Y., Zhang, Z., Yang, X.T., Zhe, S., 2021. Macroscopic traffic flow modeling with physics regularized gaussian process: A new insight into machine learning applications in transportation. *Transportation Research Part B: Methodological* 146, 88–110.

Zhang, H., Dong, H., Yang, Z., 2025a. Tsgdiff: Traffic state generative diffusion model using multi-source information fusion. *Transportation Research Part C: Emerging Technologies* 174, 105081.

Zhang, J., Mao, S., Yang, L., Ma, W., Li, S., Gao, Z., 2024. Physics-informed deep learning for traffic state estimation based on the traffic flow model and computational graph method. *Information Fusion* 101, 101971.

Zhang, K., Feng, X., Jia, N., Zhao, L., He, Z., 2022. Tsr-gan: Generative adversarial networks for traffic state reconstruction with time space diagrams. *Physica A: Statistical Mechanics and its Applications* 591, 126788.

Zhang, R., Isola, P., Efros, A.A., Shechtman, E., Wang, O., 2018. The unreasonable effectiveness of deep features as a perceptual metric, in: *Proceedings of the IEEE conference on computer vision and pattern recognition*, pp. 586–595.

Zhang, Y., Zhang, Z., Ji, J., Quiñones-Grueiro, M., Barbour, W., Gloudemans, D., Weston, C., Biswas, G., Work, D.B., et al., 2025b. Real-world deployment and assessment of a multi-agent reinforcement learning-based variable speed limit control system. *arXiv preprint arXiv:2503.01017*

Zhong, M., Lingras, P., Sharma, S., 2004. Estimation of missing traffic counts using factor, genetic, neural, and regression techniques. *Transportation Research Part C: Emerging Technologies* 12, 139–166.